Temperature Based Water Content Measurement in Mud (Soil) With Fiber Optics

by

Frederik Van Ballaer

to obtain the degree of Master of Science
at the Delft University of Technology,
to be defended publicly on Friday August 21, 2020 at 10:00 AM.

Student number:	4472403
Project duration:	March 2, 2020 - August 7, 2020
Thesis committee:	Prof. Dr. P.J. Vardon, TU Delft, Senior Supervisor
	Dr. M. Ebi Meshkati, Deltares, Supervisor
	drs. P. Doornenbal, Deltares, Supervisor
	Prof. Dr. N. Klitzsch, RWTH Aachen, Examiner
	Prof. Dr. D. Draganov, TU Delft, Examiner

TU Delft ETH zürich RWTH AACHEN UNIVERSITY Deltares

Abstract

This research has demonstrated the applicability of a DTS system to estimate the volumetric water content in saturated mud material. 2 samples of synthetically generated mud and 1 sample of natural mud from the port of Rotterdam were investigated, first by conventional methods and subsequently also with DTS. The system set-up and heating strategy were optimized by testing with different media (air, water) and with different FO coil diameters. A step-by-step approach was then designed to translate the thermal response recorded in the muds into volumetric water contents. Early- and late-time cutoffs were applied to the slope selection procedure (ΔT vs $\ln(t)$), and a mud dependent correction factor was applied to obtain the effective heat flux. The average VWC's (Θ) subsequently derived from the DTS data were in good agreement with those obtained by conventional methods (core sampling); the standard deviation in the VWC's (Θ) of all three tested muds was between 0.030 and 0.040 m^3/m^3. For saturated conditions, Sayde et al. (2010) and Striegl and Loheide (2012) published larger standard deviations of 0.046 m3/m3 and >0.050 m^3/m^3 respectively. The approach detailed in this investigation has enabled DTS to perform as a guideline on the continuous volumetric water content profile in saturated muds.

Acknowledgements

I would like to express my sincerest gratitude to my supervisor Dr. Phil Vardon and especially my primary supervisor, Dr. Ebi Meshkati, who have expertly guided me throughout this project. With his unwavering dedication, patience and enthusiasm, Ebi inspired me to stay motivated every step of the way through the ongoing COVID-19 pandemic. To my Deltares colleagues, Pieter Doornenbal, Edvard Ahlrichs and Jarno Terwindt, I am extremely grateful for your assistance, and suggestions. I wish to express my gratitude to both Harm Aantjes and 'Enabling Technologies' at Deltares for giving me this opportunity and ensuring that I was able to continue my research away from the laboratory. In addition, I wish to thank Mike van der Werf and Arjan Wijdeveld, who thought out and developed the idea that led up to this research. Most of all, I wish to acknowledge my friends and family, who's endless support has pushed me beyond my limits and helped me produce a project that I can truly be proud of.

Nomenclature

A	Area	m^2
α	Texture dependent parameter	
C	Calibration parameter	
c_s	Solid specific heat capacity	J kg^{-1} K^{-1}
C_v	Volumetric heat capacity	J m^{-3} K^{-1}
c_w	Water specific heat capacity	J kg^{-1} K^{-1}
$\Delta\alpha$	Differential attenuation	m^{-1}
ΔT	Change in temperature	°C
e	Euler constant	
η	Particle shape effect parameter	
f_a	Sand fraction	
Υ	Energy shift	J
Υ_d	Specific weight	kN m^{-3}
I_{pk}	Peak current	Amps
I_{rms}	Rms current	Amps
κ	Thermal diffusivity	m^2 s^{-1}
k	Texture dependent parameter	
χ	Particle shape effect parameter	W^{-1} K^{-1}
L	Length	m
λ	Thermal conductivity	W m^{-1} K^{-1}
λ_{sat}	Saturated thermal conductivity	W m^{-1} K^{-1}
λ_{dry}	Dry thermal conductivity	W m^{-1} K^{-1}
λ_o	Other mineral thermal conductivity	W m^{-1} K^{-1}
λ_q	Quartz thermal conductivity	W m^{-1} K^{-1}
λ_s	Solid thermal conductivity	W m^{-1} K^{-1}
λ_w	Water thermal conductivity	W m^{-1} K^{-1}
n	Porosity	
P_{aS}	Anti-stokes amplitude	
ρ_b	Dry soil bulk density	kg m^{-3}
P_S	Stokes amplitude	
ρ_w	Water density	kg m^{-3}
q	Heat flux	W m^{-1}
R	Resistance	Ω
r_m	Radial distance	m
S_r	Saturation ratio	
T	Temperature	°C
t_0	Total time of integration	s
T_0	Initial temperature	°C
t_c	Time correction factor	s
T_{cum}	Cumulative Temperature	°C s
t_m	Time of maximum temperature	s
T_m	Maximum temperature	°C
Θ	Volumetric water content	m^3 m^{-3}
Θ_{sat}	Saturated volumetric water content	m^3 m^{-3}

List of abbreviations

AC	Alternating current
AHFO	Actively heated fiber optic
DPHP	Dual probe heat pulse
DTS	Distributed temperature sensing
FDR	Frequency domain reflectometry
FO	Fiber optic
GPR	Ground penetrating radar
M1	Family of synthetic mud 1 experiments
M2	Family of synthetic mud 2 experiments
OC	Organic content
PVC	Polyvinyl chloride
R	Family of natural mud experiments
SPHP	Single probe heat pulse
TDR	Time domain reflectometry
VWC	Volumetric water content

List of figures

List of tables

Contents

1. Introduction

1.1 Problem statement for conventional water content measurement

Soil volumetric water content is described as a key state variable in near-surface hydrology, with a strong influence on the hydrological, ecological and engineering properties of the soil in question (Steele-Dunne et al, 2010, Cao et al., 2015). Conventional moisture monitoring methods (i.e. time domain reflectometry (TDR), frequency domain reflectometry (FDR), ground penetrating radar (GPR)) are capable of accurate point observations but have thus far struggled to provide continuous measurements in time and space.

In response to the limited spatio-temporal coverage achieved by conventional methods, distributed temperature sensing (DTS) with fiber optic cables has seen significant growth in popularity in the field of environmental engineering and soil monitoring. A DTS system can continuously measure temperatures along the fiber optic cable with fine temporal and spatial resolution over a significant distance (up to 30 km; temporal and spatial resolutions can be as fine as 1 second and 0.125 m, respectively). This provides a unique opportunity to closely monitor the temporal changes in temperature along the cable in a soil. The working principle of a DTS system is described in Section 3.1.

In the presence of a transient heat in a medium (such as soil) due to the diurnal radiation cycle, or due to a heat pulse transmitted from a heating source (e.g. the heating cable incorporated in the fiber optic cable, known as active DTS or AHFO), the thermal response (i.e. the heating and cooling trend) can be related to the thermal properties of the medium i.e.: thermal conductivity and volumetric heat capacity. Thermal conductivity is a measure of the amount of heat per unit time passing through a unit cross-sectional area under a thermal gradient in the direction of heat flow. Volumetric heat capacity is the amount of heat required to raise the temperature of a given volume of material by 1 K.

The thermal conductivity and specific heat capacity are mainly a function of water content, porosity, composition and type of solid particles and the presence of important constituents such as gas and organic content. Hence, by monitoring the thermal response along the DTS fiber optic cable, potentially valuable information on its water content can be determined. However, this is not a simple and straightforward task and challenges regarding the selection of appropriate heating strategies and an optimal data processing approach to translate the thermal response into water content remain. In this research, through a series of systematic lab-scale tests, we will evaluate the applicability of DTS systems for high resolution soil moisture measurements and establish a set of guidelines to transform the thermal response into meaningful volumetric water content data.

1.2 Application of DTS to determining soil moisture content

Distributed Temperature Sensing (DTS) using a fiber optic cable was first developed in the early 1980s. The oil industry was the first to deploy this technology for detecting leaks and fires in oil and gas pipeline networks. The first general application of this technology for environmental monitoring was in geothermal monitoring in the late 1990s. In the mid-2000s, DTS was increasingly used for hydrological and hydrogeological purposes (e.g. Hartog, 1983 and Kersey, 2000).

In the past decade, the feasibility of using a DTS system to measure the volumetric water content (VWC) in soil has been demonstrated by both laboratory and field tests (e.g. Weiss, 2003, Sayde et al. (2010), Ciocca et al., (2012), Striegl and Loheide (2012), Apperl et. al., (2019)).

Sayde et al. (2010) used an empirical approach to demonstrate the capability of DTS in detecting the soil water content in the laboratory with an accuracy of 0.001 m3/m3 in soils with a VWC of 0.05 m3/m3. Further testing revealed an increase of the standard deviation up to 0.046 m3/m3 for soils with higher water contents (VWC = 0.41 m3/m3). This was later corroborated by Apperl et al. (2019) who used the dual probe heat pulse method (DPHP) to attribute the loss of accuracy to a reduction in sensitivity of soil thermal properties to VWC, as the soil in question approaches saturation. Similar results came from an empirical field investigation by Striegl and Loheide (2012) where the root mean square error (RMSE) of VWC estimates exceeded 0.050 in soils under wet conditions (VWC > 0.31 m3/m3).

A laboratory study based on the single probe heat pulse method (SPHP) featuring a lysimeter conducted by Ciocca et al. (2011) indicated larger discrepancies (>0.1 m3/m3) between AHFO-DTS and conventional capacitance-based probes at lower water contents than at higher water contents (precision between 0.01-0.035 m3/m3). These seemingly 'contradictory' results compared to previous studies were linked to the nature of the model used to interpret the recorded thermal response.

Sayde et al. (2010) aptly argued that the accuracy of a DTS system in water content characterization therefore not only depends on the design and operational protocol of the system but also on the post processing approach used to translate the measured thermal response to water content.

1.3 Objectives

Despite the apparent success of DTS in characterizing soil water content, both in the laboratory and on a field to watershed scale, significant challenges remain. One of the most important of challenges is the selection procedure of an optimized heating strategy and a subsequent systematic data processing approach that would transform a soil's thermal response into accurate VWC measurements.

Our research aims to bridge the knowledge gap discussed in the preceding section by attempting to answer the following research question:

- *What is the optimum heating strategy, data processing and modelling approach for DTS to obtain volumetric water content measurements and what is the associated accuracy?*

Considering the application of DTS in submerged conditions, such as those encountered in ports, water ways, estuary systems, our research will be primarily focused on mud under saturated conditions.

1.4 Structure of thesis

This research is split into the following sections: 1. Introduction and problem statement, 2. Literature review of the models and methods available to translate DTS data into VWC (Θ), 3. The materials and methods used in the experimental set-up, 4. The experimental design of the tests performed, 5. The results and discussion, 6. The conclusion with recommendations and improvements.

2. Literature review

This section of the report is dedicated to the investigation of models available in literature that translate a thermal response captured in DTS into VWC (Θ) data.

2.1 Statistical models

Cumulative Temperature model:

Empirical in nature, the cumulative temperature model relies on an integrated thermal response variable 'T_{cum}' [°C s] that varies monotonically with VWC (Θ) and is determined by equation (1) below (Sayde et al. 2010 and 2014).

$$T_{cum} = \int_0^{t_0} \Delta T \, dt \qquad (1)$$

where t_0 is the total time of integration and ΔT is the temperature increase measured by the DTS with respect to the reference temperature taken prior to the heat pulse. By fitting a function through the T_{cum} values obtained from DTS data versus independent VWC (Θ) measurements taken by 'conventional' means (TDR soil moisture probes), this model produces soil-specific relationships between ΔT and VWC (Θ). A similarly used parameter is the maximum DTS recorded temperature during a heat pulse, known as T_{max}. T_{max} and T_{cum} share the same approach to VWC (Θ) estimation with certain advantages and limitations to both. For more information on the cumulative temperature model, consult the relevant literature by Sayde et al. (2010 and 2014) and Duminda et al. (2018).

Characteristic Temperature model:

Similar to the cumulative temperature model, the characteristic temperature model provides an empirical approach to estimating VWC (Θ) from DTS temperature measurements. The characteristic temperature is a range of ΔT's averaged over a time period where the temperature in response to heating is tapering off. These characteristic temperatures are then plotted against the various VWC (Θ) measurements performed by point soil moisture probes to yield a soil-specific relationship. Consult literature by Striegl and Loheide (2012) for a more detailed approach to the characteristic temperature model.

2.2 Volumetric Heat Capacity (C_v) models

In an infinite, isotropic, homogenous medium with radial heat flow and no soil water flux, the conduction of heat is described by Carslaw and Jaeger (1959) as:

$$\frac{\partial T}{\partial t} = \kappa\left(\frac{\partial^2 T}{\partial r^2} + \frac{1}{r}\frac{\partial T}{\partial r}\right) \quad (2)$$

where T is temperature [°C]; t is time since the start of heating [s]; κ is thermal diffusivity [$m^2\ s^{-1}$] and r [m] is the radial separation from the line heat source. Carslaw and Jaeger (1959) then formulate the solution to (2) for a constant flux supplied to an infinitely long line source with infinitesimally small radius as:

$$\Delta T(r,t) = \frac{Q}{4\pi\kappa t}\exp\left(\frac{-r^2}{4\kappa t}\right) \quad (3)$$

where $Q = q/C_v$, q is the heat flux [W m^{-1}] going through the source and C_v is the volumetric heat capacity of the surrounding medium [J m^{-3} K^{-1}]. By differentiating (3) with respect to time and setting the resulting equation to 0, the maximum temperature change C_v at time t_m and radial distance r_m is found (Campbell et al. 1991). Through a few further manipulations detailed in Campbell et al. (1991), equation 3 can be re-arranged for C_v yielding:

$$C_v = \frac{q}{e\pi r_m^2 \Delta T_m} \quad (4)$$

From equation (4), it may be observed that to determine volumetric heat capacity from the thermal response to a heat pulse, the parameters ΔT_m, r_m and q must be known. In distributed temperature sensing, equation (4) may be approximated through the dual probe heat pulse approach. The thermal response to a line heat source is monitored some fixed distance (r_m) away by a sensing cable and the maximum temperature rise (ΔT_m) is recorded.

The soil volumetric heat capacity (C_v) can be approximated as the weighted sum of the heat capacities of its individual constituents (de Vries 1963; Kluitenberg, 2002).

$$C_v = c_s\rho_b + c_w\rho_w\theta \quad (5)$$

where c_s [J kg^{-1} K^{-1}] is the specific heat capacity of solids, c_w [J kg^{-1} K^{-1}] is the specific heat capacity of water and ρ_b, ρ_w [kg m^{-3}] are the dry soil bulk density and pore water density respectively. By determining the soil solid density and soil solid heat capacity, equation (5) may then be arranged to provide us with an estimate of the VWC (Θ) in place.

In literature, studies have suggested improvements to (4) as the DTS designs often don't meet the requirements to be considered an instantaneous pulse delivery system to an infinite line heat source. For models based on more realistic geometric descriptions such as a cylindrical heat source of finite length and radius, consult literature by de Vries (1952); J. H. Knight and Kluitenberg (2004); Benítez-Buelga et al. (2014).

2.3 Thermal Conductivity (λ) models

Unlike C_v models, thermal conductivity-based models require a DTS system with just a single sensing probe, serving as both the line heat source and measuring device. DTS results are translated to VWC (Θ) in a 2-step approach, going first from $\Delta T \rightarrow \lambda$ and then from $\lambda \rightarrow \Theta$.

I) From thermal response to thermal conductivity ($\Delta T \rightarrow \lambda$)

The thermal conductivity can be derived from the analytical solution to Fourier's conduction of heat equation (2) featuring an infinite line heat source in an isotropic, homogenous medium with radial heat flow and constant initial temperature T_0 (de Vries, 1952; Carslaw and Jaeger, 1959; Shiozawa and Campbell, 1990). The change in temperature $T - T_0$ at radial distance r may then be expressed as:

$$T - T_0 = -\left(\frac{q}{4\pi\lambda}\right) Ei\left(\frac{-r^2}{4\kappa t}\right) \tag{6}$$

with Ei the exponential integral function. As a special function on the complex plane, exponential integrals are inconvenient to process on most spreadsheets and calculators. Shiozawa and Cambell (1990) demonstrate an exponential integral function may be expanded as follows:

$$\begin{aligned} -Ei(a) &= \int_a^{\infty} (1/u) exp\,(-u) du \\ &= -\gamma - \ln(a) + a - \frac{a^2}{4} + \cdots \end{aligned} \tag{7}$$

where the argument a is $\left(\frac{-r^2}{4\kappa t}\right)$, γ is Euler's constant and u is the variable of integration. For $a \ll 1$, all higher order terms (HOT) after the logarithm in (7) contribute negligibly and may be dropped, reducing (6) to:

$$T - T_0 = \left(\frac{q}{4\pi\lambda}\right)\left[-\gamma - \ln\left(\frac{-r^2}{4\kappa t}\right)\right] = \left(\frac{q}{4\pi\lambda}\right)[c + \ln(t)] \tag{8}$$

for sufficiently large t. Variable c represents the grouping of constant variable terms such as radial distance r, thermal diffusivity κ and Euler's number γ. Equation (8) demonstrates how a linear regression between change in temperature $T - T_0$ and the logarithm of time $\ln(t)$ may yield the thermal conductivity λ of the heated medium.

For small values of t, the argument in the exponential integral is not $\ll 1$ and thus equation (8) incorrectly approximates (7) by neglecting meaningful higher order terms. Further errors in application originate from the heat source's finite radius and imperfect contact resistance (Shiozawa and Campbell, 1990). To account for these errors, a correction factor t_c may be introduced to equation (8) as described by de Vries (1952); Shiozawa and Campbell (1990):

$$T - T_0 = \left(\frac{q}{4\pi\lambda}\right)[\ln(t + t_c)] + d, \text{ for } t < t_h \quad (9)$$

with d being a constant and t_h the duration of the heat pulse. In reality, t_c is set-up dependent and often not known a priori, so instead, early time data is excluded from the analysis of the measured thermal response and linear regression (Bristow, 2002).

Once the heat pulse is turned off, a similar equation to (9), but with an additional term accounting for the loss of q at $t > t_h$, can be formulated for the cooling phase:

$$T - T_0 = \left(\frac{q}{4\pi\lambda}\right)[\ln(t + t_c') - \ln(t - t_h + t_c')] + d' \text{ , for } t > t_h \quad (10)$$

The second logarithmic term in (10) represents the introduction of an imaginary heat sink equal and opposite in magnitude to the applied heat pulse q. t_c' and d' may differ from the t_c and d terms encountered in equation (9) of the heating phase. After simplification through the properties of logarithms, (10) becomes:

$$T - T_0 = \left(\frac{q}{4\pi\lambda}\right)\left[\ln\frac{(t+t_c')}{t-t_h+t_c'}\right] + d' \text{ , for } t > t_h \quad (11)$$

A regression between $T - T_0$ and $\ln\frac{(t+t_c')}{t-t_h+t_c'}$ would allow for the determination of the medium's thermal conductivity λ from the cooling phase. Shiozawa and Campbell (1990) propose averaging the thermal conductivity estimates from both the heating and cooling phase to obtain the best results, though other studies have given preference to either heating or cooling (Ciocca et al., 2011; Sakaki et al., 2019)

Additionally, there is a lack of clarity on the slope selection procedure from which the thermal conductivity is estimated. For the heating phase, early time data is often excluded from the analysis (Bristow, 2002), but the decision of where exactly to perform the cut-off remains undefined. Furthermore, in a study by Sakaki et al. (2019) both early- and late-time data is removed from the analysis; the latter to avoid effects of the boundaries of the system set-up. The approach demonstrated in this paper will attempt to clarify the analysis procedure as well as the cut-off times.

II) Thermal conductivity – Volumetric Water Content ($\lambda \rightarrow \Theta$)

The thermal conductivity of a complex composite material such as a soil can be considered a function of the thermal properties, volume fraction, and spatial distribution of its constituents. The most prevalent $\lambda \rightarrow \Theta$ models in literature are outlined below.

Johansen Model (1975) Model

A saturated soil may be approximated as a two-phase medium consisting of solid particles and water. With this notion in mind, Johansen (1975) proposed the following relationship between total soil thermal conductivity λ of unsaturated soils and the normalized thermal conductivity K_e, based on the λ values at dry and saturated conditions:

$$\lambda = (\lambda_{sat} - \lambda_{dry})K_e + \lambda_{dry} \quad (12a)$$

For coarse-textured soils:

$$K_e = 0.7\log(S_r) + 1.0, \text{ for } S_r > 0.05 \quad (12b)$$

While for fine textured-soils:

$$K_e = \log(S_r) + 1.0, \text{ for } S_r > 0.1 \quad (12c)$$

S_r being the saturation ratio and commonly defined as Θ/Θ_{sat}. From (12b, c) it is evident that the original model was not designed for completely dry soils ($S_r < 0.05$). Due to the complex nature of soil structure, it is inadequate to simplify a soil to a set of layers with individual thermal conductivities in series or in parallel. Therefore, to estimate λ_{sat}, a geometric mean equation weighted by constituents was established (Farouki, 1981).

$$\lambda_{sat} = {\lambda_s}^{1-n}{\lambda_w}^{n} \quad (13)$$

where λ_s [W m^{-1} K^{-1}] is the thermal conductivity of the soil solids, λ_w [W m^{-1} K^{-1}] is the thermal conductivity of the water and n the soil porosity. Johansen described a further geometric mean equation for λ_s, based on the fraction q and thermal conductivity λ_q of quartz vs that of other common minerals λ_o.

$$\lambda_s = {\lambda_q}^{q}{\lambda_o}^{1-q} \quad (14)$$

λ_o is set at 2.0 W m^{-1} K^{-1} for soils with a quartz content $q > 0.2$ and 3.0 W m^{-1} K^{-1} for soils featuring a quartz content $q \leq 0.2$ (Lu et al., 2007).

Finally, λ_{dry} is determined using a semi-empirical equation with bulk density ρ_b and soil solid density (2700 kg m^{-3}) as main components:

$$\lambda_{dry} = \frac{0.135\rho_b + 64.7}{2700 - 0.947\rho_b} \quad (15)$$

With all parameters now defined, equation (12a) can be re-arranged to solve for volumetric water content Θ.

For fine-textured soils:

$$\Theta = \Theta_{sat} * 10^{(\frac{\lambda-\lambda_{dry}}{\lambda_{sat}-\lambda_{dry}}-1)/0.7}, \text{ for } S_r > 0.05 \quad (16a)$$

For coarse-textured soils:

$$\Theta = \Theta_{sat} * 10^{(\frac{\lambda-\lambda_{dry}}{\lambda_{sat}-\lambda_{dry}}-1)}, \text{ for } S_r > 0.1 \quad (16b)$$

Côté and Konrad (2005) Model

In 2005, research published by Côté and Konrad detailed an updated version of Johansen's 1975 model that distinguishes between 4 soil textures (gravel/coarse sand, medium/fine sand, silty/clayey soils, organic soils) and describes the $\lambda \rightarrow \Theta$ relationship across all water contents ($0 \leq S_r \leq 1$). In their model, Côté and Konrad (2005) retained the relationship expressed by (12a) but defined the normalized thermal conductivity K_e as follows:

$$K_e = \frac{kS_r}{1+(k-1)S_r} \quad (17)$$

where k is the texture dependent parameter taken as 4.60, 3.55, 1.90, 0.60 for gravel/coarse sand, medium/fine sand, silty/clayey soils and organic soils respectively. Further adjustments were made with regards to the representation of both λ_{dry} and λ_s, whilst Johansen's definition for λ_{sat} remained unchanged.

$$\lambda_{dry} = \chi * 10^{-\eta n} \quad (18)$$

In equation (18), n is the soil porosity whilst χ [W^{-1} K^{-1}] and η are the particle shape effect parameters. Respectively, Côté and Conrad (2005) assigned values of 1.70 W^{-1} K^{-1} and 1.80 for crushed rocks, 0.75 W^{-1} K^{-1} and 1.20 for mineral soils and 0.30 W^{-1} K^{-1} and 0.87 for organic soils.

The geometric mean equation for λ_s is based on the individual thermal conductivities and volume fractions of each of the rock-forming mineral present (instead of just quartz fraction q). The model therefore requires a complete soil classification.

$$\lambda_s = \sum_{n=1}^{i} \lambda_i^i \tag{19}$$

Lu et al. (2007) Model

Lu et al.'s model (2007) draws on both Johansen's original model from 1975 and the augmented version published by Côté and Conrad in 2005. It is argued that the relationship between K_e and S_r remains poorly represented in fine soils and at low volumetric water contents (Lu et al., 2007). The resulting model features a soil texture dependent parameter α, as well as a shape parameter equal to 1.33:

$$K_e = exp\left\{\alpha\left[1 - S_r^{(\alpha-1.33)}\right]\right\} \tag{20}$$

Furthermore, λ_{dry} is redefined yet again, this time by a linear relationship with soil porosity:

$$\lambda_{dry} = -an + b \tag{21}$$

where a and b are empirical parameters determined from the $\lambda_{dry}\ vs\ n$ plot.

Nikoosokhan et al. (2015)

Nikoosokhan et al.'s (2015) iteration of the Johansen (1975) model includes 2 new linear relationships of both the dry λ_{dry} and saturated thermal conductivity λ_{sat} with the sand fraction f_a and dry soil specific weight γ_d [kN m^{-3}].

$$\lambda_{dry} = 0.087 f_a + 0.019\gamma_d \tag{22}$$

$$\lambda_{sat} = 0.53 f_a + 0.1\gamma_d \tag{23}$$

The dry soil specific weight γ_d is computed as $9.8 * \rho_b$ with ρ_b representing the soils dry bulk density and 9.8 the gravitational acceleration. Nikoosokhan et al. (2015) then employs equation (17) as described by the Côté and Konrad (2005) model, but with a key change to k, the texture-dependent parameter:

$$k = 4.4f_a + 0.4 \quad (24)$$

Like the dry and saturated thermal conductivities, k is set to vary linearly with the soil's sand fraction. Rearrangement of 12a) then yields the relationship between the thermal conductivity of a soil with its volumetric water content.

Other less common methods include the Camillo and Schmugge (1981) model and the de Vries Model (1963). The former is a simple λ model with few input parameters whilst the latter is a complex λ model where each of the soil's constituents are weighted individually, along with the inclusion of the gaseous phase interactions (air molar density, latent heat of vaporization, vapor diffusivity, etc.). For a more detailed description, consult literature by Camillo and Schmugge (1981) and de Vries (1963).

2.4 Justification of model selection

Currently, there is no established method for data interpretation of AHFO-DTS measurements (He et al., 2018). Selecting an appropriate model is dependent on both the set-up and objective of the investigation.

As this research is focused on the mud in the saturated state, the statistical models introduced in Section 2.1 are less attractive as they rely on the testing of materials with a wide range of water contents ($0 < \Theta < \Theta_{sat}$) before they produce a meaningful $T_{cum} \rightarrow \Theta$ calibration curve. Furthermore, the key limitation to the use of these models is the required calibration process which has, to date, employed extensive laboratory experimentation for a single soil (Benítez Buelga, 2014) which is both costly and time-consuming.

Although volumetric heat capacity C_v has been recognized as linearly linked to the volumetric water content (de Vries, 1963), there are some significant drawbacks in the application of the DPHP method that make the C_v model class inappropriate for this investigation. A closer look at equation (4) reveals that a small error in r would result in a significant error in C_v, making the model extremely sensitive to the spacing between 2 FO sensors (Kluitenberg et al., 1993, 1995). Furthermore, to register an observable change in temperature at the sensing cable, the FO cables must be spaced very closely together (He et al., 2018), resulting in a relatively large cable radii to cable spacing ratio. Apperl et al. (2019) states that the cables and their multi-layered structure will then influence the measured thermal response in such a way that the derived heat capacity is a combination of the individual heat capacities of not only the soil but also the set-up. The common errors/uncertainties associated to the DPHP method are magnified for DTS applications as the systems involved are orders of magnitude larger.

Thermal conductivity models have the advantage of only needing a single fiber optic cable. Furthermore, much effort has already been made to develop $\lambda(\Theta)$ models with easily obtained soil parameters as those mentioned in Section 2.3 (de Vries, 1963; Johansen, 1975; Côté and Konrad, 2005; Lu et al., 2007). These are fundamental steps in developing an optimized heating strategy and subsequent data processing approach and are therefore preferable for an investigation of this type.

2.5 Selected thermal conductivity model

Model selection: $\Delta T \rightarrow \lambda$

Although Shiozawa and Campbell (1990) suggest using a combination of the heating and cooling phase to determine the soil thermal conductivity, Weiss et al. (2003) demonstrated in a study that the thermal conductivity obtained in the cooling phase is consistently larger than that obtained in the heating phase. It is suggested that this might be the result of local soil drying and relocation of pore water from higher temperature regions to lower temperature regions. The phenomenon of vapor transport (both heat and liquid) in soils is documented in an extensive study by Farouki (1986). To avoid complicating the analysis with the effects of vapor transport, this research will therefore focus solely on the heating phase of the thermal response registered by DTS.

Model selection: $\lambda \rightarrow \Theta$

Considering that the experiments will be performed on saturated muds only, we may assume that the VWC (Θ) and the porosity n are equal ($\Theta = \Theta_{sat}$). Similarly, the overall soil thermal conductivity λ and the saturated soil thermal conductivity λ_{sat} are equal, such that equation (13) from Johansen's original model can be rewritten as:

$$\lambda_{sat} = \lambda = {\lambda_s}^{1-\Theta} {\lambda_w}^{\Theta} \tag{25}$$

And subsequently rearranged for Θ:

$$\Theta = \frac{\ln\left(\lambda/\lambda_s\right)}{\ln\left(\lambda_w/\lambda_s\right)} \tag{26}$$

For each mud, λ_s will be determined from independent laboratory tests, whilst λ_w is taken as approximately 0.594 W m^{-1} K^{-1} at 20 °C (Lu et al., 2007). This formulation of the $\lambda \rightarrow \Theta$ relationship avoids uncertainty associated with shape and fitting parameters as seen in the Côté and Konrad (2005), Lu et al. (2007) and Nikoosokhan et al. (2015) models.

3. Materials and methods

3.1 DTS Working principle

The DTS consists of a controller unit (laser source, pulse generator, optical module, receiver and micro-processor) and a fiber optic (FO) cable as line-shaped "temperature sensor". The fiber optic cable consists of a glass core of about 50 µm in diameter (typically made of quartz glass) covered with glass cladding (typically made of B_2O_3:SiO_2). The working principle of DTS is as follows: a pulse generator launches pulses of light into the fiber optic cable at a wavelength between 800 to 1600 nm (slightly beyond the visible spectrum) and pulse duration of about 10 ns (Suárez et al., 2011). As a light pulse travels along the cable, it encounters impurities in the glass core's crystal structure. This causes a fraction of the incident light to reflect to the controller unit along the same path as the incident light, which is referred to as a "backscattering event" (Selker et al., 2006a). Three main types of backscattering may occur in DTS, namely Rayleigh, Raman and Brillouin scattering.

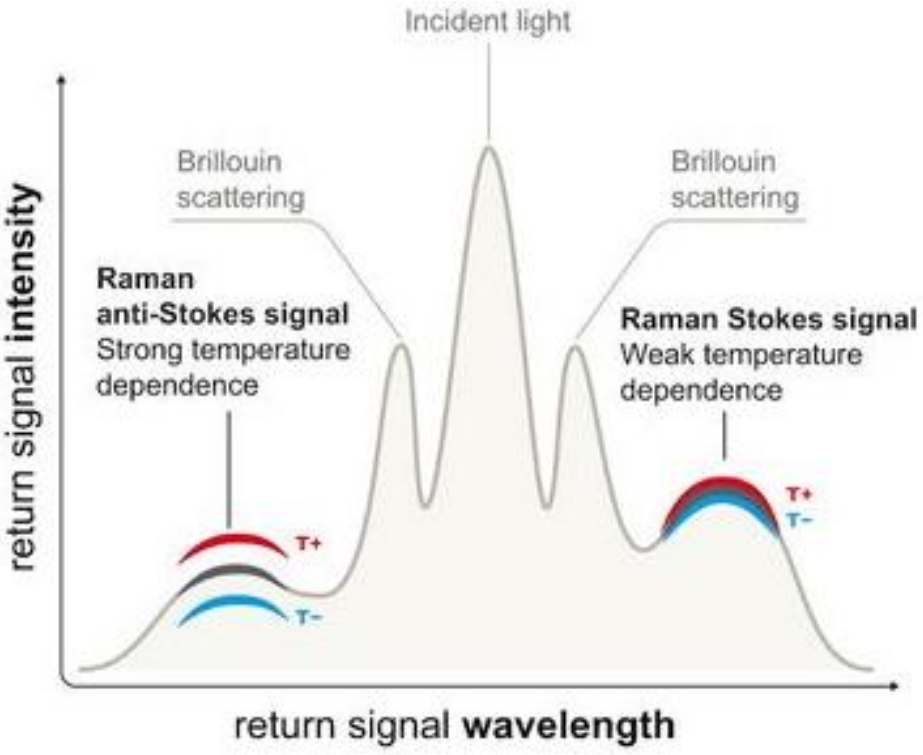

Fig. 1. Rayleigh, Brillouin and Raman back-scattering in optical fibers. The Raman Stokes and anti-Stokes components are highlighted according to their respective temperature dependence (source: reprinted from APSensing.com).

The intensity of the anti-Stokes component is strongly influenced by thermal excitation, whilst the Stokes component remains relatively unaffected (Fig. 1). This way, the ratio between the anti-Stokes and Stokes wavelengths of the Raman scattering can be used to estimate the temperature along the fiber. The location of the temperature measurement along the cable is calculated using the travel times of the incident and scattered light. A comprehensive review of the theoretical foundation of DTS systems can be found in Selker et al. (2006b).

3.2 Muds tested

Experiments were performed on 2 variations of synthetically compiled saturate mud and a single batch of saturated natural mud obtained from the port of Rotterdam.

3.2.1 Synthetic mud

The synthetic mud samples were made by mixing OCMA and FT-S1 according to the proportions displayed in Table 1.

Components	Mass [kg]
OCMA	133.0
FT-S1	66.5
Water	500.0

Table 1. Constituents of synthetic mud mixture.

The OCMA is sodium activated bentonite produced by Cebo Holland, with a particle size distribution of min. 99% < 150 µm and a specific weight of 2300 kg m^{-3}. The FT-S1 is a mixture manufactured by Sibelco Deutschland featuring a mineral composition of 64% disordered Kaolinite, 10% Mica and 19% Quartz with a specific weight of 2500 kg m^{-3}. The equivalent spherical diameter of particles in the FT-S1 mixture are at least 99% < 63 µm. The resulting synthetic mud has a shear strength of 0.4kPa and was split into two batches. To facilitate loading of the system and avoid the formation of air pockets, both batches were further diluted with water to a final wet bulk density of 1200 kg m^{-3} and 1150 kg m^{-3} respectively.

3.2.2 Natural mud (Port of Rotterdam)

The natural mud originates from dredging operations performed in the Port of Rotterdam. Though this mud has not yet been analyzed for mineral content or chemical composition, it is expected to consist of predominantly marine silts and sand originating from the North Sea mixed with alluvial silts from the Rhine and Meuse (Kirichek et al., 2018). Significant amounts of organic content may also be present.

3.3 Experimental Set-up

3.3.1 DTS unit

The DTS unit used for this research was the Ultima S (Silixa Ltd, UK), capable of discerning temperatures up to 0.01 °C with a sampling interval of 0.125m. The measurements were performed with 2 single-ended configurations set up in reverse (channel 1 and 2), with an acquisition time of 2 seconds per channel. The laser would alternatively pulse in channel 1 and channel 2 so that each channel registers a data point every 4 seconds.

Two external PT100 sensors were connected to the DTS unit to provide reference temperatures for the calibration procedure described in Section 5.1.2. The first PT100 sensor was placed in the calibration bath at room temperature, whilst the second was placed inside the water column of the set-up.

3.3.2 Fiber optic cable

The FO used is a multi-component sensing cable (FiberConnect® GL AT-V(ZN)H(ZN)H n) manufactured by Leoni FO in Germany. The cable spans approximately 160m in length and has an outer diameter of 1.8mm (0.0018m) with numeric coding marked on the outside. As in Fig. 2, the FO consists of 4 sub-cables; each holding a buffered fiber, aramid strain relief elements and a halogen-free, flame-retardant (FRNC) sub-cable jacket. The cable itself also has aramid strain relief elements and an outer wall of FRNC. Only 2 of the 4 buffered fibers were used for the investigation; 1 representing data for channel 1 on the DTS unit and 1 representing data for channel 2.

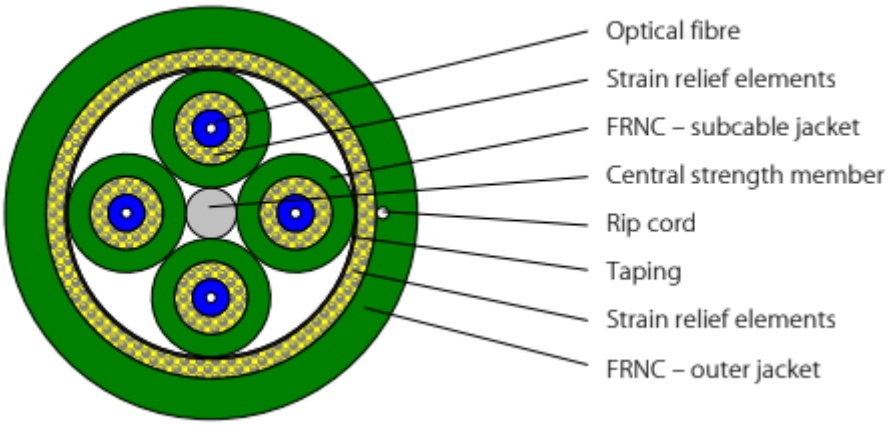

Fig. 2. Profile view of the fiber optic cable with individual components labeled (source: reprinted from leoni-fiber-optics.com).

3.3.3 Power supply unit

The power supply unit used in the investigation is a 1975 Regel-Trenn-Transfromator that provides alternating current (AC) to produce an output power of 800 Watts with a maximum current of 3.5 amperes. The model is manufactured by Grundig Electronics in Germany.

3.3.4 Heating cable

The heating cable is a stainless-steel core enveloped by a protective silicone coating. The cable has an outer diameter of 3.0 mm and total length of 38m. The total resistance of the cable is 59.9 ohms without extension cord and 60.4 ohms with extension cord. Table 2 gives an overview of the thermal properties belonging to the components that make up the FO and heating cables.

Medium	Thermal Conductivity [W m^{-1} K^{-1}]	Specific Heat Capacity [J kg^{-1} K^{-1}]
Heating cable core	54.0	465
Heating cable outer jacket	0.2	100
FO core	2	1430
FO aramid strain relief elements	0.04	1420
FO sub- and outer jacket	0.196	1565

Table 2. Thermal properties of selected set-up components (Bakx et al., 2019).

3.3.5 Set-up for heating tests

The materials described above were compiled into the configuration shown in Fig. 3. Fig. 4 depicts a conceptual schematic view of the setup. The testing column is a 1.4 m tall Plexiglass cylinder with a diameter of 0.394 m. Two vertical support rods are mounted in parallel; one in the center of the column and the other 0.05 m away (measured from core to core). The center pole (Pole 1) was initially an 8 mm diameter rod of M8 threaded galvanized steel but was later replaced with a hollow PVC tube with a diameter of 32 mm, wall thickness of 2 mm and insulating foam filling in its center. The second pole (Pole 2) is also a water filled PVC tube, but has a diameter of 16 mm and a wall thickness of 1 mm.

The center pole is wrapped by the heating cable from bottom to top, with a coil density of 3 coils per centimeter of pole. The FO cable is then wrapped around this coiled heating cable from a height of 0.05 m to 1.11 m measured from the bottom of the column. The coiling of FO cable is approximated to be constant and as tight as possible without overlap. The second pole is wrapped solely by FO cable and in similar fashion to the center pole.

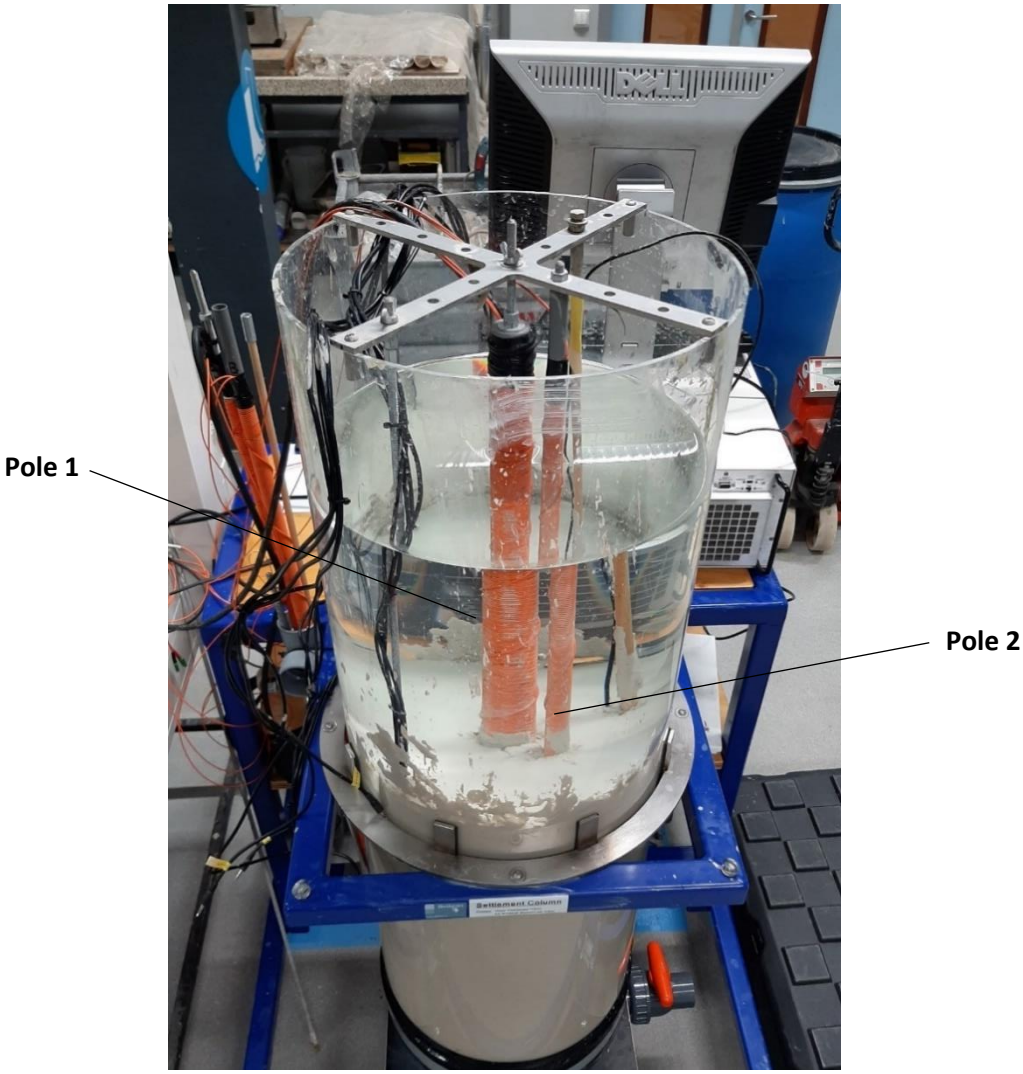

Fig. 3. The experimental column with Pole 1 and Pole 2 mounted in a batch of synthetic mud. FO coils (orange) span a vertical height of 0.05 – 1.11 meters measured from the bottom of the column.

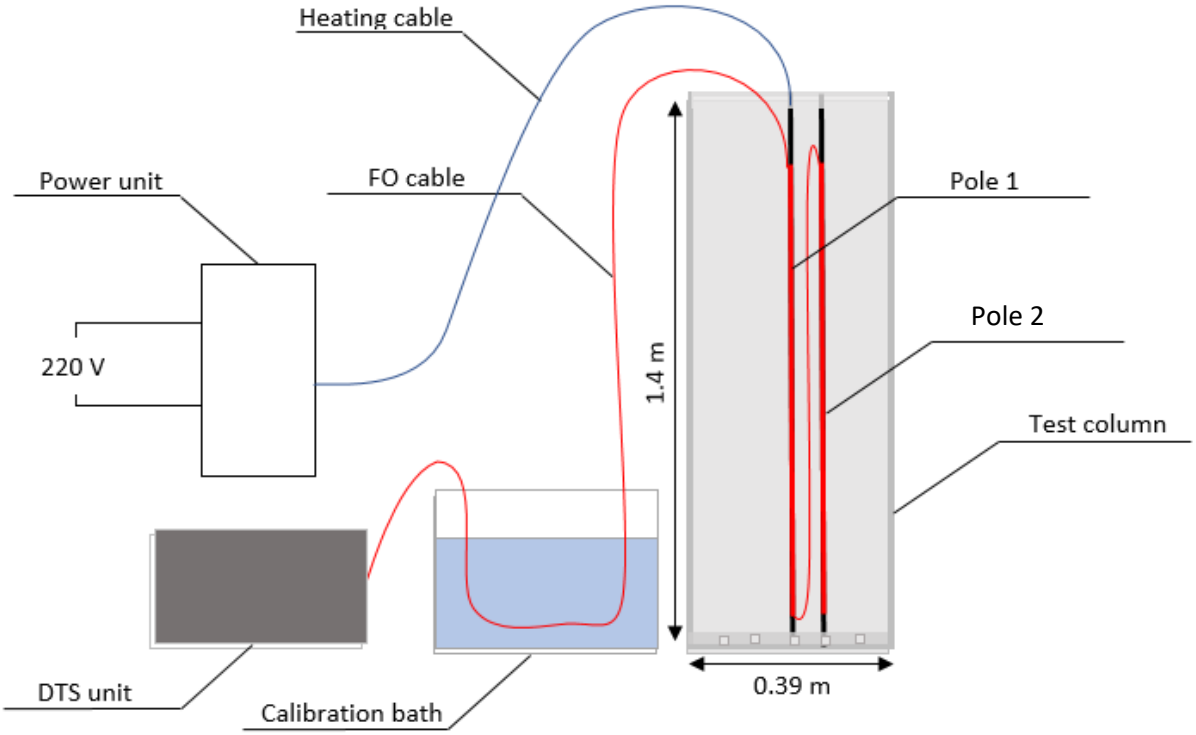

Fig. 4. Schematic profile of the system set-up. FO coils span the poles from 0.05 m to 1.11 m height. Important features include the DTS unit, Power unit, FO cable, heating cable and test column. The FO is wrapped from top to bottom; first going along Pole 1 and then onto Pole 2, before returning along the exact same trajectory.

Upon analysis of the initial experiments performed in air/water, it was decided that main tests on synthetic mud types and natural mud would be performed under a modified version of the original set-up. Below are the dimensions of the fiber optic configuration for both the initial and modified set-up (Table 3 and Table 4).

Original Configuration	FO Cable Section [m]	Total Length [m]
Calibration bath	1.0 – 9.0	8.0
Pole 1 (heating + sensing)	11.1 – 34.6	23.5
Pole 2 (sensing only)	48.4 – 78.4	30.0
Pole 3 (sensing only)	85.1 – 115.1	30.0

Table 3. Original FO configuration with important cable sections highlighted.

Modified Configuration	FO Cable Section [m]	Total Length [m]
Calibration bath	2.0 – 14.0	12.0
Pole 1 (heating + sensing)	15.0 – 81.0	66.0
Calibration bath	84.0 – 98.0	14.0

Table 4. Modified FO configuration with important cable sections highlighted. The FO passes through the calibration bath, onto the Pole 2nd finally back through the same calibration bath. Sensing poles 2 and 3 were placed too far away from heating pole 1 to record a distinguishable rise in temperature and are therefore removed for the modified configuration.

4. Experimental design and procedure

4.1 Active distributed temperature sensing measurements

A complete active DTS measurement cycle consists of 3 phases: I) the pre-pulse reference phase, II) the heating phase and III) the cooling phase. In phase I, the DTS unit is switched on and left to record temperature that, after averaging, will serve as the reference temperature T_0. Phase II starts with the initiation of the heat pulse. A heat flux q is applied to the system for a pre-determined duration and the corresponding temperature rise is recorded. Phase III is the section of the cycle where the heat pulse has been terminated and the temperature ideally recovers to the pre-pulse reference temperature T_0. This cycle is repeated for every experiment conducted with the DTS system. Fig. 5 is a graphical representation of a single DTS cycle.

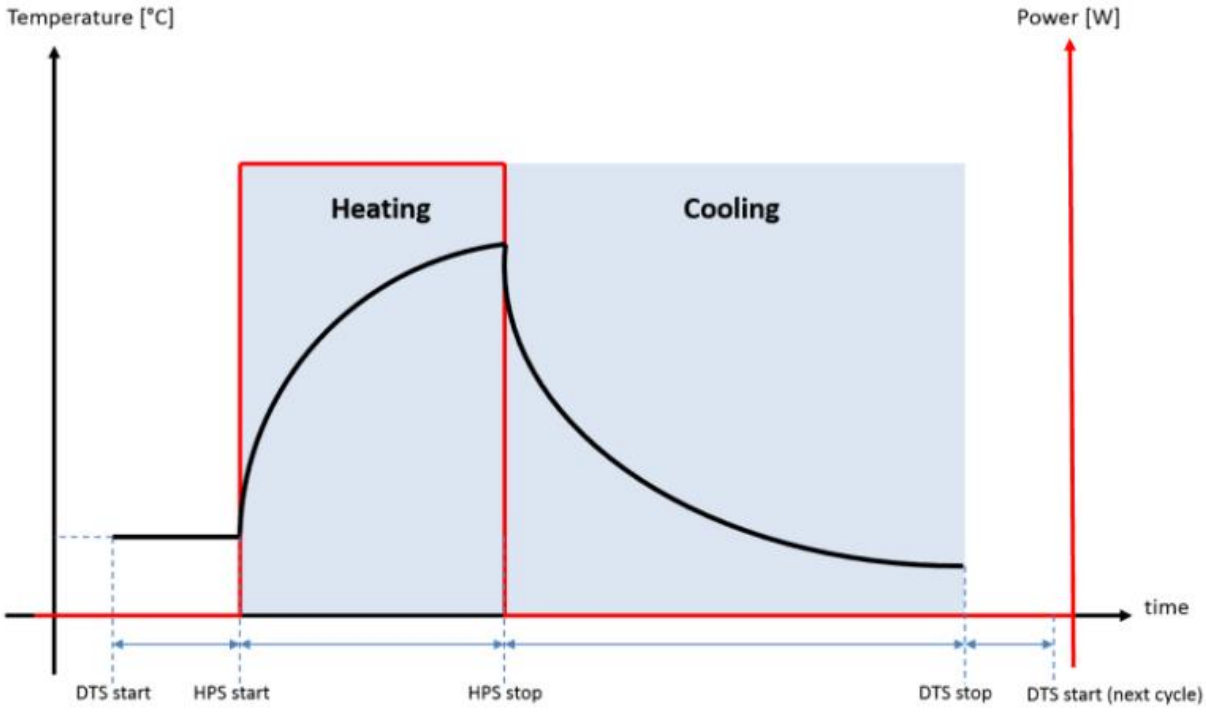

Fig. 5. Complete DTS cycle with 3 phases highlighted. Phase I is the pre-pulse section where a reference temperature is established. Phase II is the section where the heat pulse is applied, Phase III is the cooling section where the heat pulse has been terminated and the temperature of the medium is returning to the reference temperature (source: reprinted from silixa.com).

4.1.1 Air

Preliminary tests with air as the sole experimental medium were performed to determine potential FO anomalies (splices, connections, damage, etc.). If the system is damaged or performing poorly, this will show up as a noticeable drop in signal on a stokes/anti stokes intensity plot. Given air's low thermal conductivity, it is also a good medium to record large temperatures and allows the investigator to determine a maximum safe current that may be applied to the system without damaging the FO. Furthermore, these experiments serve to test the current produced and resistance recorded by the power unit and heating cable respectively. Using the power unit, currents ranging from 0.75-2.2 amps were tested.

4.1.2 Water

The DTS experiments performed on water were designed to extend the set-up optimization process. Multiple heating strategies with a variety of magnitudes and durations were tested to get an approximate overview of the associated temperature increase expected in the synthetic and natural muds. Based on the results, a selection of suitable currents and heat pulse durations could then be made. Every experiment was performed on a column filled with 1.00 m of water at room temperature. Table 5 lists the 12 heating strategies tested.

Experiment code	Peak current [amps]	Duration [s]
W1	0.75	300
W2	1.0	300
W3	1.1	300
W4	1.2	300
W5	1.3	300
W6	1.4	300
W7	1.5	300
W8	1.6	300
W9	1.6	600
W10	1.8	300
W11	2.0	300
W12	2.2	300

Table 5. List of heating strategies tested on a water-filled column. Currents applied ranged from 0.75 to 2.2 amps, for a duration of between 300 – 600 seconds.

From W10 onwards, the modified set-up described in Section 3.3.5 was implemented to investigate the effect of a larger diameter support pole on the spread (standard deviation) of the temperatures recorded with DTS. The hypothesis here is that a larger diameter support pole encourages a larger bend radius for the FO, so that there is a reduction in attenuation caused by macrobending (Jay, 2010).

4.1.3 Synthetic mud

The purpose of using synthetic muds prior to their natural variants (e.g. mud from ports) is to determine the performance of the DTS system and processing approach in a 'controlled' environment. The synthetic mud selected has no organic polymers and is expected to have negligible amounts of settlement, compaction and minimal heterogeneity. By eliminating some of the complicating factors usually encountered when investigating (natural) mud, the synthetic tests are expected to produce data on the accuracy of the DTS and processing approach with respect to obtaining a VWC (Θ) profile.

The column is filled with 0.6m of synthetic mud (M1 – 1200 kg m^{-3} and later M2 – 1150 kg m^{-3}) and topped with 0.4m of water to ensure no drying/cracking takes place in between tests. Fig. 6 is a side view profile of the column when loaded with mud and water. Since the FO spans the poles from 0.05 – 1.11 meters, the bottom 0.05 m of mud is not profiled by the DTS.

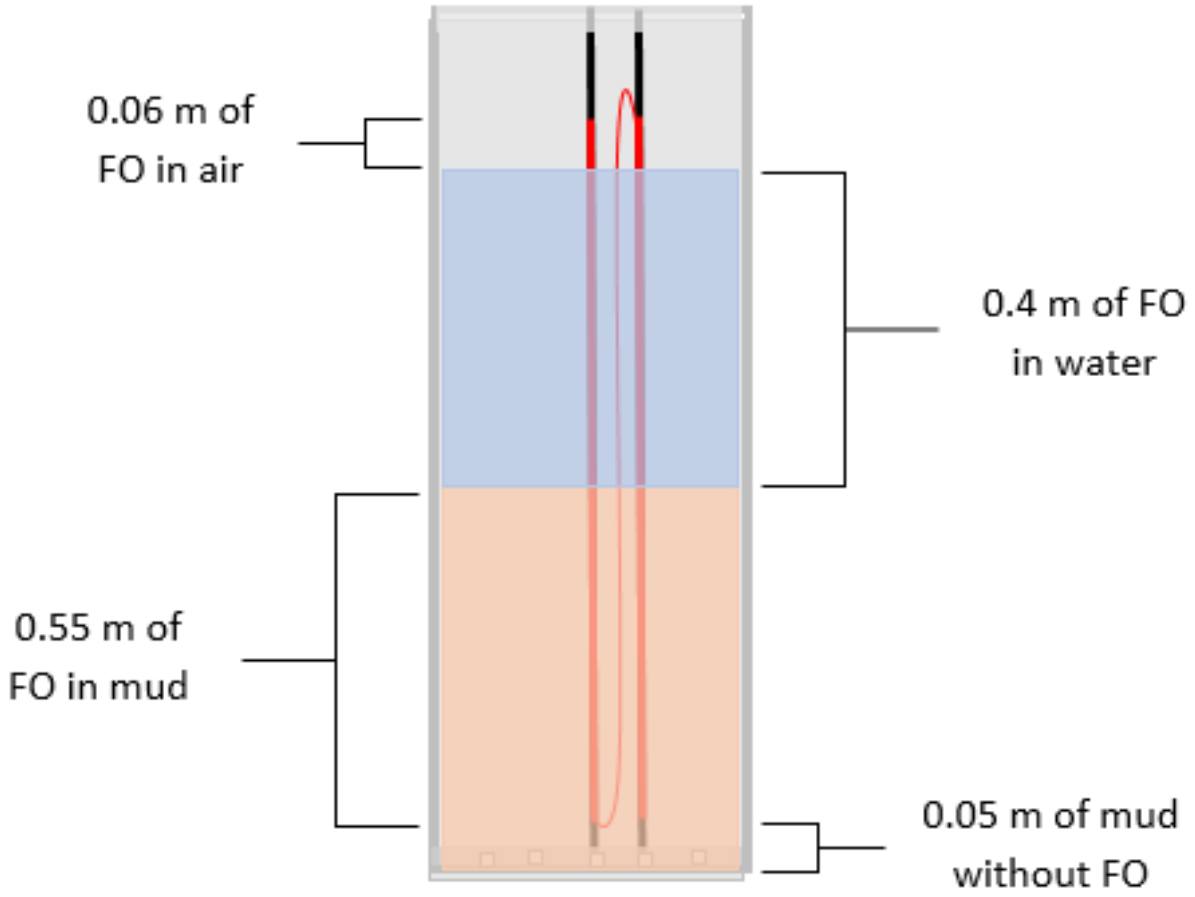

Fig. 6. Vertical integration of the column for a mud experiment. The column is filled with 0.6 m of mud and topped by 0.4 m of water. The FO coiling spans a height of 0.05 – 1.11 m, measured from the bottom of the column.

Synthetic mud 1 – M1

Table 6 below summarizes the tests conducted on synthetic mud M1. The letter S in experimental code refers to 'synthetic', followed by a number which refers to the test number. In total 9 tests on synthetic mud M1 were planned. S6-M1 and S8-M1 were not processed due to errors in the data transfer procedure.

The heating strategies in Table 6 and Table 7 were selected based on the outcome of preliminary tests described in Section 4.1.1 and 4.1.2. Current amplitudes below 1.4 were neglected due to the limited rise in temperature in water, whilst current amplitudes above 1.8 were avoided to ensure the integrity of the FO cable remained intact. By independently repeating every chosen current magnitude (1.4, 1.6, 1.8 amps) and duration (150, 300, 600 seconds) three times, the results of each test may be verified by two others.

Experiment code	Peak current [amps]	Duration [s]
S1-M1	1.4	150
S2-M1	1.6	150
S3-M1	1.8	150
S4-M1	1.4	300
S5-M1	1.6	300
S6-M1*	1.8	300
S7-M1	1.4	600
S8-M1*	1.6	600
S9-M1	1.8	600

*Table 6. List of heating strategies tested on a column filled with synthetic mud 1. A total of 9 experiments were planned, with currents spanning 1.4 – 1.8 amps and durations ranging from 150 to 600 seconds. *S6-M1 and S8-M1 were not performed.*

Synthetic mud 2 – M2

Table 7 below summarizes the tests conducted on synthetic mud M2. The letter S in experimental code refers to 'synthetic', followed by a number which refers to the test number. In total 9 tests on synthetic mud M2 were planned.

Experiment code	Peak current [amps]	Duration [s]
S1-M2	1.4	150
S2-M2	1.6	150
S3-M2	1.8	150
S4-M2	1.4	300
S5-M2	1.6	300
S6-M2	1.8	300
S7-M2	1.4	600
S8-M2	1.6	600
S9-M2	1.8	600

Table 7. List of heating strategies tested on a column filled with synthetic mud 1. A total of 9 experiments were planned, with currents spanning 1.4 – 1.8 amps and durations ranging from 150 to 600 seconds.

4.1.4 Natural mud (Port of Rotterdam)

Once the synthetic mud tests are concluded, the investigation proceeds with natural mud obtained from dredging works in the port of Rotterdam. This step is important because it represents the application of the developed system in a more 'realistic' environment. The synthetic mud will be loaded into the testing column exactly like its synthetic counterparts (see Fig. 6) and will be subjected to the same heating strategies, for the sake of comparison (see Table 8).

Natural mud (port of Rotterdam) – R

Experiment code	Peak current [amps]	Duration [s]
R1	1.4	150
R2	1.6	150
R3	1.8	150
R4	1.4	300
R5	1.6	300
R6	1.8	300
R7	1.4	600
R8	1.6	600
R9	1.8	600

Table 8. List of heating strategies tested on a column filled with natural mud from the Port of Rotterdam. A total of 9 experiments were planned, with currents spanning 1.4 – 1.8 amps and durations ranging from 150 to 600 seconds.

4.2 Direct measurements

The direct measurements in this research refer to the conventional methods that exist to determine first thermal conductivity and then VWC (Θ). The thermal conductivity tests will be performed by thermal needle probe and the VWC (Θ) measurements will be performed by core sampling and oven drying (see section 4.2.1 and 4.2.2).

4.2.1 Thermal needle probe

Determining the thermal conductivity of each mud prior to DTS testing is important to get an approximate number for the soil solid thermal conductivity λ_s as found in equation (13), without the need for a full mineralogical study. In combination with the VWC (Θ) obtained from core sampling, λ_s can be obtained for every mud type investigated.

The thermal conductivity of each tested mud was determined with a thermal needle probe (TP02) in accordance with the guidelines described in ASTM D5334-14. The set-up consists of a hollow cylindrical tube encasing a thermocouple and heating wire cast in Epoxy (Fig. 7). The needle is inserted into the mud by gently pushing it in. Starting at stable reference temperature, a current supplied to the heating wire warms the probe and surrounding mud sample. The thermal response of the sample is then used to extract the sample's thermal conductivity. Consult ASTM D5334-14 for more details.

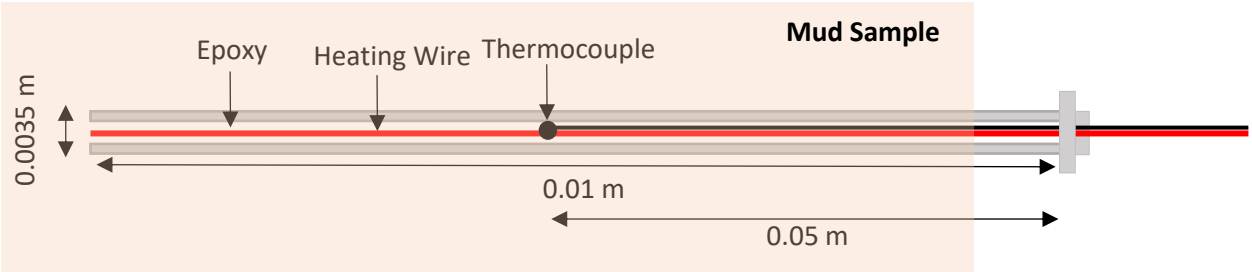

Fig. 7. Schematic overview of the thermal needle probe. The heating wire and thermocouple are cast in the center of a hollow tube that is inserted into the sample.

For all thermal needle probe experiments, 2 batches of each mud were prepared (6 total). Every batch was then tested 3 times each, so that every mud has 6 thermal conductivity measurements to average over.

4.2.2 Core sampling

Sediment core sampling is the straightforward process of oven-drying representative soil samples to get an idea of the VWC (Θ) that was present pre-drying. For this research, a standard Beeker sampler manufactured by Eikelkamp Soil & Water was used. Upon the completion of all DTS experiments, the mud in the column (0.6m in height) would be sampled immediately and divided into 6 equal parts of 0.1 m. Direct height measurements before and after experiments were performed showed almost no settling in synthetic mud and very little settling in the mud from the port of Rotterdam. The parts would be individually weighted and then oven dried for 24 hours at 105 °C. Upon reweighing, the reduction in mass would be represent the mass of water initially in place. The 6 VWC's (Θ) obtained would be each be representative of a 0.1 m section of the column and are assigned a height equal to the midpoint of their respective sections. As a result, we have 6 VWC's (Θ) at 6 distinct points in height (0.05, 0.15, 0.25, 0.35, 0.45 and 0.55 meters)

5. Results and Discussion

5.1 DTS data pre-processing

5.1.1 Raw distributed temperature sensing data

The Silixa Ultima S records and subsequently stores the temperatures (DTS and PT100) as well as the Stokes and anti-Stokes intensities in a single XML file for every pulse emitted, separated by channel. These XML files are then loaded into the DTS Viewer Lite® software as an entire folder, where the user can cycle through every time interval recorded for the duration that the DTS system was active. The XML files are then loaded into a python data store object, from which temperatures, times and even specific cable sections can be called. One may also choose to convert the XML files into a single aggregated CSV file that is then transformed directly into a Data frame in python. Although both channel 1 and 2 data were available, a bad splice/connector in the latter caused significant data loss and thus the processing presented is based solely on channel 1.

As a result, any further processing is performed on single-ended measurements. Research by Tyler et al. (2008) has shown that for investigations with relatively short FO cable lengths (<500 m), single-ended measurements provide a higher accuracy in temperature than their double-ended variants. The primary reason for this being that at short distances from the source, averaging 2 measurements (forward and backward) returns a signal with a larger average noise component than that of the single measurement.

The Silixa Ultima S (Silixa Ltd., UK) has a sampling interval of 0.125 m and sampling resolution of 0.54m, where the sampling resolution is defined by the manufacturer as the length required to record 80% of a temperature step change. However, with a coil density of approximately 62 coils per vertical meter, the section of FO on the poles of this set-up reported temperature measurements every 0.002m (vertically).

Now that only channel 1 data is considered, the temporal sampling time of the raw data is approximately 4 seconds. The temporal sampling time of a DTS system is positively correlated with the accuracy in temperature measurements computed. However, as sampling time is increased, rapidly changing temperature signals become more difficult to capture and resolve. Additionally, the limited duration of the heat pulses tested (600 seconds maximum) require sufficient data in time to produce a representative thermal response. Finally, as our set-up features a particularly small diameter FO (0.0018m) with limited cladding and strength elements, it is expected that any thermal response to an induced heat pulse propagates quickly enough so that a small sampling time is appropriate (Tyler et al., 2009).

5.1.2 Raman Spectra DTS Calibration

Calibration is a crucial step in obtaining accurate temperature data, as it accounts for the inherent signal attenuation and temperature offset of the DTS system. To understand the procedure, we must consider how DTS performs the conversion from the Stokes/anti-Stokes ratio to temperature data:

$$T(z) = \frac{\gamma}{ln\frac{P_S(z)}{P_{aS}(z)} + C - \Delta\alpha z} \tag{27}$$

In equation (27), $P_S(z)$, $P_{aS}(z)$ and $T(z)$ represent the Stokes power, anti-Stokes power and computed temperatures at position z [m]. γ represents the energy shift between a photon at incident ray wavelength and the back-scattered Raman photon, C is a dimensionless calibration parameter unique to the DTS unit/laser combination used and $\Delta\alpha$ is the differential attenuation between the Stokes and anti-Stokes signals (Hausner et al., 2011). More information on the input parameters of equation (27) can also be found in Hausner et al. (2011).

During calibration, γ, C and $\Delta\alpha$ are estimated from the comparison of P_S and P_{aS} with external temperature measurements at reference location(s). The reference location in this research was an insulated calibration bath filled with water and kept at room temperature, away from direct sunlight. FO sections that passed through the calibration bath are 2 – 14 m and 84 – 98 m, as displayed in Fig. 8 below.

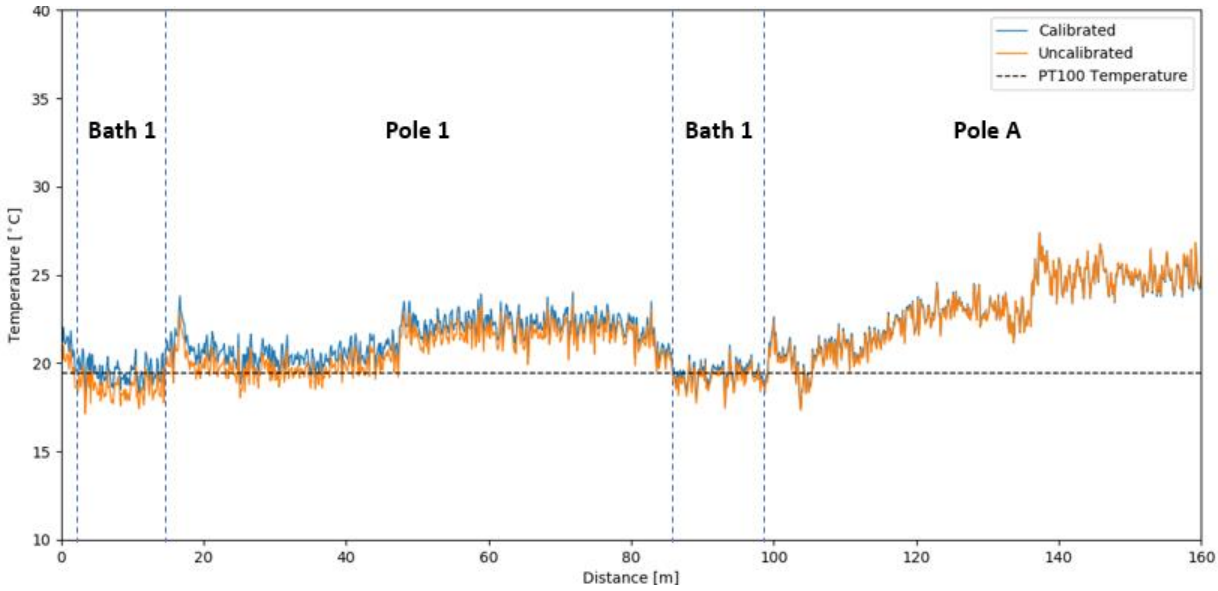

Fig. 8. Temperature plot across the entire FO cable length for both calibrated and uncalibrated measurements. Calibration was performed with reference temperatures obtained from the external PT100 temperature sensor located in calibration bath 1 (2 – 14 m and 84 – 98 m).

The calibration procedure selected is dependent on the system set-up, FO cable length and desired degree of accuracy. Single-ended set-ups like the one described in this research, where the Stokes and anti-Stokes intensities are only measured from one end of the fiber, are then also subjected to single-ended calibration. For this, the 'dtscalibration' python package developed by des Tombe et al. (2020) was used.

For single-ended DTS calibration, the differential attenuation $\Delta\alpha$ between the Stokes and anti-Stokes intensities is assumed constant along the entire fiber length. The drawback of single-ended calibration is therefore that it risks neglecting the effect of splices and connectors (regions with varying $\Delta\alpha$) along the fiber, leading to a temperature offset (des Tombe et al., 2020). With this in mind, the internal reference temperature, which is separated from the FO by a connector, is neglected from the calibrated section. Furthermore, by checking the Stokes and anti-Stokes intensity plots of initial experiments (e.g. air tests) carefully, it was ensured that no significant splicing occurred in channel 1 (see Fig. 9).

5.2 Preliminary DTS experiments

Prior to running DTS experiments on mud material, the column was first tested with air and water to prevent future data loss and to ensure the system was running smoothly. Consult Section 4 for more details on the experimental design.

5.2.1 Air tests

Several DTS cycles were performed in air, with currents ranging between 0.75 amps to 2.2 amps. The maximum temperature recorded at 2.2 amps was 70.1 °C. To ensure the FO wasn't compromised during coiling or heating, the Stokes and anti-Stokes intensities are plotted along the entire FO cable length, where splices and subsequent signal loss are characterized by sharp drops. In Fig. 10, a significant drop in intensity is observed around x = -30 meters; likely the result of the internal connector inside the DTS unit. The FO section used for data analysis is the range between x = 0 m and x = 160 m, where there are no sudden drops to be reported. It is therefore appropriate to proceed with single-ended calibration (see Section 5.1.2). Similar snapshots were investigated over the course of the research to ensure the set-up remained intact.

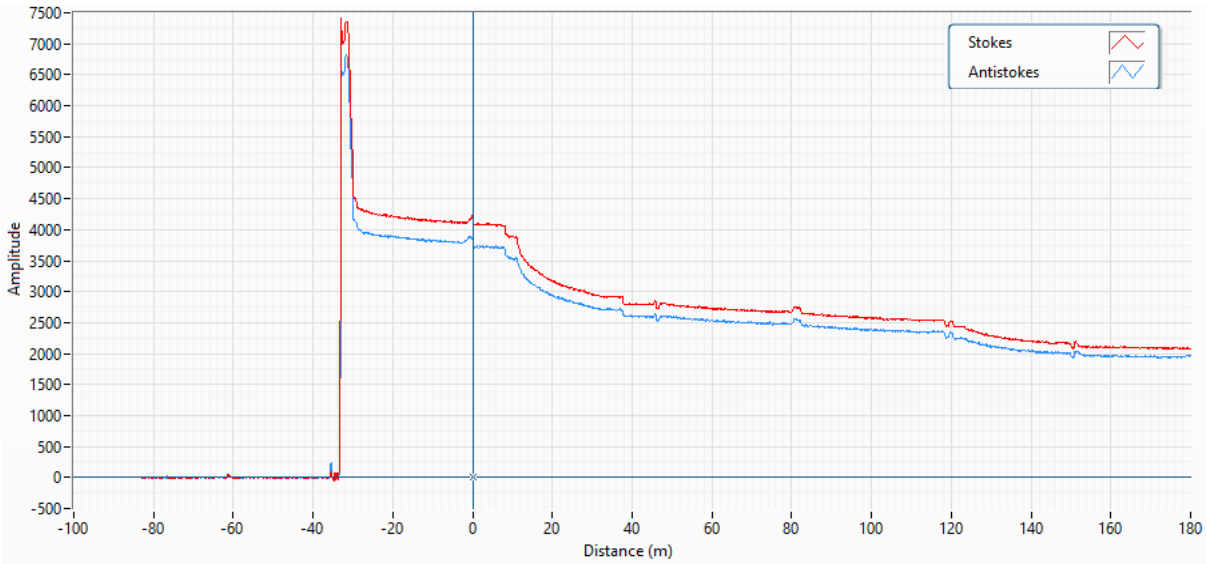

Fig. 9. DTS Viewer Lite interface showing the Stokes and anti-Stokes intensities along the FO length. The FO cable exits the DTS unit at x = 0 m. Single ended calibration is performed from x = 0 to x = 160 meters. The effect of the internal connector is represented by a significant loss in intensity around -30m. It may be observed that there is no evidence of a connector or splice on the section of FO considered for data processing (0 – 160 m).

5.2.2 Water tests

A water-filled column was used to investigate the performance of the FO cable at different points along the set-up. The effect of coiling, heating and winding diameter (diameter of support pole) on the DTS measurements is detailed below.

Effect of coiling:

Of interest was the accuracy of measurements on the coiled poles compared to measurements taken in the calibration water bath. The 'coiling' effect is demonstrated below in Fig. 10, where the standard deviation in temperature measurements on both Pole 1 and Pole 2 is significantly higher than for temperatures recorded in the water bath, prior to the initiation of a heat pulse. This increase in uncertainty is almost certainly the result of macrobending, where the FO experiences increased attenuation (Jay, 2011). How much the attenuation increases depends on the bend radius as well as the number of coils and may therefore be mitigated by using a larger diameter pole for future experiments.

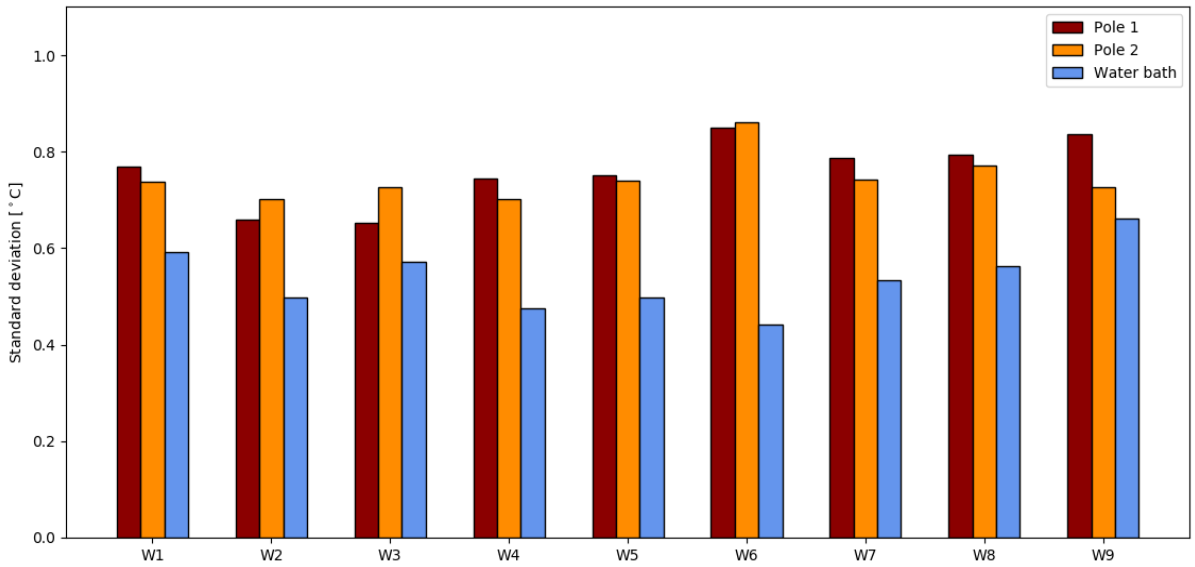

Fig. 10. Standard deviation in temperature along the fiber optic cable prior to heating. W1-W9 represent a range of experiments tested on a water filled column. The water bath is the calibration bath, Pole 1 is a structure wrapped with heating cable and FO cable, Pole 2 is wrapped only with FO cable.

Effect of heating:

It was hypothesized that, other than coiling, the accuracy of DTS measurements is also dependent on the rate of temperature change of the surroundings that the FO is attempting to record. In other words, a system at rest is expected to produce temperature readings with a lower variation than those recorded in a system that is experiencing a heat pulse. By comparing the standard deviations of temperatures recorded in the water bath with those recorded on Pole 1 and Pole 2 right after system was heated, it can be observed that this hypothesis is correct. Since Pole 2 is far enough removed (0.05m) from the heating element wrapped around Pole 1, its data may be approximated as recorded in a system at rest. Fig. 11 below illustrates the combined effect of coiling and heating on the accuracy of FO measurements taken on Pole 1.

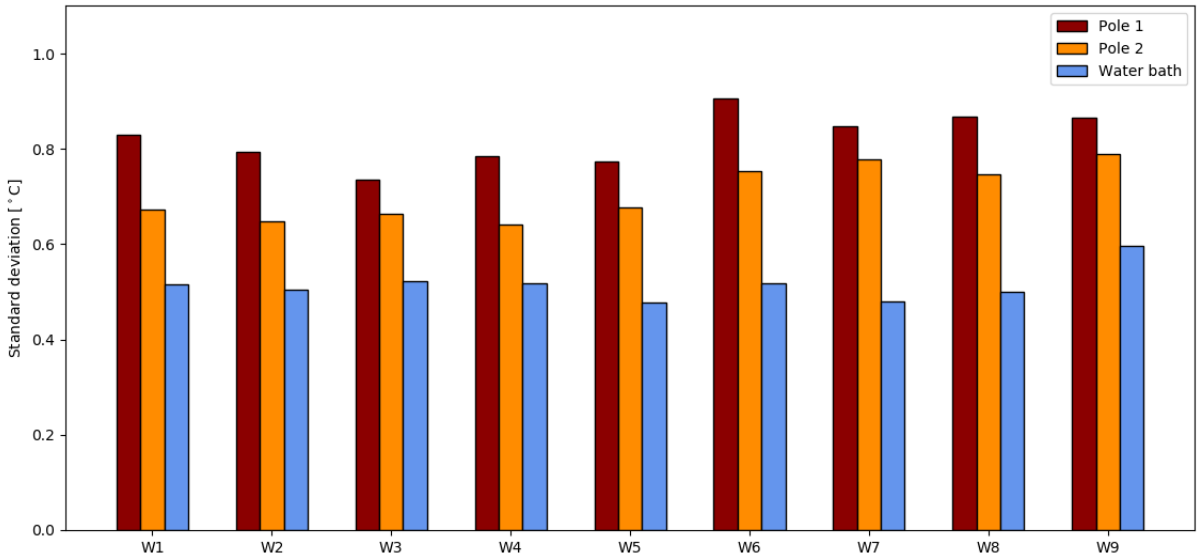

Fig. 11. Standard deviation in temperature along the fiber optic cable 300s after initiating a heat pulse. W1-W8 represent a range of experiments tested on a water filled column with durations of 300s and currents of between 0.75 - 1.8 amps. The water bath is the calibration bath, Pole 1 is a structure wrapped with heating cable and FO cable, Pole 2 is wrapped only with FO cable.

Effect of pole diameter:

In an attempt to reduce the attenuation caused by coiling, the set-up was modified such that Pole 1 had its diameter increased from 0.008m to 0.032m. Experiments W10 – W12 were performed with the modified set-up and the standard deviations in temperature recorded on Pole 1 were subsequently plotted for all water tests. Fig. 12 demonstrates that the modified set-up produces results with lower variability. Any further tests will therefore be performed with the modified set-up.

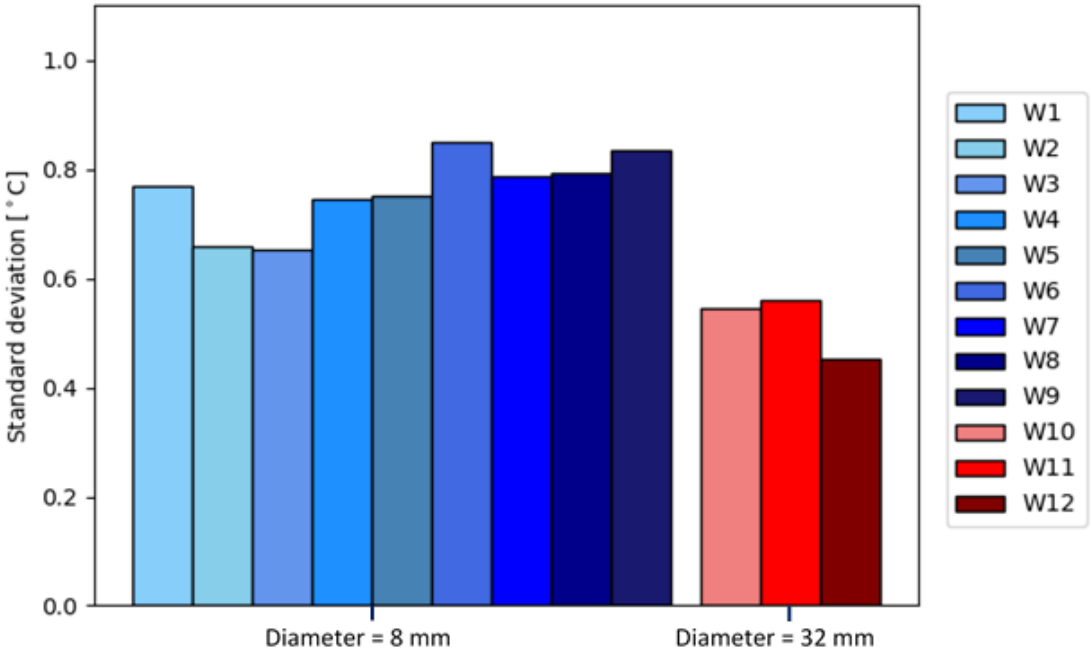

Fig. 12. Standard deviation along the fiber optic cable in the water bath and on Pole 1 during heating. W1-W9 were performed with the original Pole 1 (D = 0.008 m), whilst experiments W10 - W12 were performed with the modified Pole 1 (D = 0.032 m).

5.3 Mud Experiments

The data processing and modeling approach selected for this research can be divided into 2 main sections: the $\Delta T \rightarrow \lambda$ step and the $\lambda \rightarrow \theta$ step. ΔT itself is obtained from the thermal response of the DTS system as the rise in temperature recorded since the start of the heat pulse. From there, a linear regression is performed on the semi-log plot of $\Delta T \; vs \; \ln(t)$, and the thermal conductivity is extracted from the slope as per equation (9). However, to ensure the appropriate slopes are selected, 2 cutoff times (early and late) are implemented that serve to isolate the section of the thermal response where the effects of thermal conductivity dominate. Meanwhile the mud thermal conductivity, VWC (θ) and eventually solid thermal conductivity are obtained from direct measurements so that equation (26) has all the necessary input parameters required for the $\lambda \rightarrow \theta$ step. The direct measurements are then also used to predict the effective heat flux and the discrepancy between this value and the heat flux calculated from the geometry of the system. To account for this discrepancy, a set-up dependent heat flux correction factor is then introduced and, finally the DTS predicted VWC (θ) may be computed. Further explanations of these steps follow in the sections below.

5.3.1 Direct measurements

The objective of conducting direct measurements in parallel to DTS measurements is to obtain reference values of the thermal conductivity λ and volumetric water content of all mud samples that DTS based results can then be compared to. Furthermore, these results are required to determine the mud-specific solid thermal conductivity λ_s, an important unknown parameter that enables the $\lambda \rightarrow \theta$ step as described by equation (26). Note that as stated in Section 2, given that all tests are conducted under saturated conditions, $\lambda = \lambda_{sat}$.

Thermal needle results:

Medium	Thermal conductivity [W m^{-1} K^{-1}]	Source
Water (20 °C)	0.597	Lu et al., 2007
Clay	2.920	Nagy, 2014
Sand (Quartz)	8.800	Nagy, 2014
Organic content	0.250	Nagy, 2014

Table 9. Thermal conductivities of common mud constituents

For all three muds investigated (synthetic mud 1 - M1, synthetic mud 2 - M2, natural mud from the port of Rotterdam - R), two independent batches were prepared for conventional thermal conductivity measurements. Using a thermal needle, every batch was tested 3 times such that there are 6 thermal conductivity values recorded for all 3 mud types. Table 10, Table 11 and Table 12 display the results of these tests, their average across 6 trials and also the solid and water content of the mud used for each trial. Solid and water contents were obtained by first determining wet and dry bulk densities through oven drying, and then solving for their volumes. Solid content is defined as the mass of solids divided by the density of solids, scaled by total volume of sample and similarly water content is defined as the mass of water divided by the density of water, also scaled by total sample volume. Trial 4 for the natural mud resulted in an anomalously low thermal conductivity for only minor changes in solid/water content and was henceforth discarded from the averaging procedure for natural mud.

Synthetic mud 1:

	TC1 [W m^{-1} K^{-1}]			TC2 [W m^{-1} K^{-1}]			Average thermal conductivity [W m^{-1} K^{-1}]
	Trial 1	Trial 2	Trial 3	Trial 1	Trial 2	Trial 3	
	0.75	0.75	0.75	0.73	0.75	0.75	0.75
Solid content (m^3m^{-3})	0.124	0.123	0.122	0.116	0.122	0.118	
Volumetric water content (m^3m^{-3})	0.876	0.877	0.878	0.884	0.878	0.882	

Table 10. Thermal conductivities obtained from the thermal needle test. TC1 and TC2 represent the 2 batches of synthetic mud 1 that were then tested 3 times each. Solid content and water content of the individual samples is listed as well.

Synthetic mud 2:

	TC1 [W m^{-1} K^{-1}]			TC2 [W m^{-1} K^{-1}]			Average thermal conductivity [W m^{-1} K^{-1}]
	Trial 1	Trial 2	Trial 3	Trial 1	Trial 2	Trial 3	
	0.69	0.70	0.70	0.68	0.69	0.70	0.69
Solid content (m^3m^{-3})	0.093	0.093	0.093	0.093	0.094	0.094	
volumetric water content (m^3m^{-3})	0.907	0.907	0.907	0.907	0.906	0.906	

Table 11. Thermal conductivities obtained from the thermal needle test. TC1 and TC2 represent the 2 batches of synthetic mud 2 that were then tested 3 times each. Solid content and water content of the individual samples is listed as well.

Natural mud from Port of Rotterdam:

	TC1 [W m^{-1} K^{-1}]			TC2 [W m^{-1} K^{-1}]			Average thermal conductivity [W m^{-1} K^{-1}]
	Trial 1	Trial 2	Trial 3	Trial 1	Trial 2	Trial 3	
	0.85	0.85	0.86	0.76*	0.86	0.86	0.86
Solid content (m^3m^{-3})	0.219	0.224	0.220	0.221	0.221	0.221	
Volumetric water content (m^3m^{-3})	0.781	0.776	0.780	0.779	0.779	0.779	

*Table 12. Thermal conductivities obtained from the thermal needle test. TC1 and TC2 represent the 2 batches of natural mud that were then tested 3 times each. *Trial 1 from batch 2 of the natural mud produced an anomalous result and was subsequently discarded from the averaging calculation. Solid content and water content of the individual samples is listed as well.*

To comment on the plausibility of the determined thermal conductivities, we consider the thermal conductivities of the soil constituents as listed in Table 9. The synthetic muds both feature large water contents and are thus expected to have a thermal conductivity close to that of water (0.597 $Wm^{-1}K^{-1}$). Synthetic mud 2 has more water and thus a lower thermal conductivity. The solid particles are clay minerals. Natural mud has a lower water content and is therefore expected to have a higher thermal conductivity, as is seen in the results (0.86 W m^{-1} K^{-1}). Although organic content (OC) itself has a very low thermal conductivity (0.25 $Wm^{-1}K^{-1}$) and is likely also part of the natural mud mix, the presence of highly conductive quartz grains in the form of sand balances out the effect of OC on the overall thermal conductivity of the natural mud.

Core sampling results:

VWC (Θ) for synthetic mud 1, 2 and natural mud was determined using a Beeker sampler and oven drying at 105 °C for 24 hours (the mass difference post-drying, divided by the total volume of the tested sample). Synthetic muds tests were performed on a column loaded with 0.60 m of material. The natural mud tests were performed on a column loaded with approximately 0.47 m (instead of 0.60 m) of material so one data point at 0.55 m is missing in Table 13 displayed below.

Every core is sub-sampled at 0.1m intervals, thus producing VWC's (Θ) for 6 points in height along the pole, measured from the bottom of the column. The VWC's (Θ) are assumed to be homogenous in the horizontal plane so that every data point represents a slice of the sampled mud. The results are displayed in Table 13 below. Due to a lack of natural mud from the port of Rotterdam, there was not enough material to sample above 0.5m and thus there is no data for this height.

Height above bottom of column [m]	**Volumetric water content Θ [m^3/m^3]**		
	Synthetic mud 1 [M1]	Synthetic mud 2 [M2]	Natural mud [R]
0.55	0.881	0.913	/*
0.45	0.879	0.907	0.780
0.35	0.877	0.907	0.780
0.25	0.877	0.907	0.772
0.15	0.877	0.906	0.763
0.05	0.879	0.907	0.774

*Table 13. VWC (Θ) for synthetic mud 1, 2 and natural mud determined using a Beeker sampler and oven drying at 105 °C for 24 hours. *The natural mud tests were performed on a column loaded with approximately 0.47 m (instead of 0.60 m) of material so one data point at 0.55 m is missing.*

Solid Thermal Conductivity:

Another parameter to estimate for the mud types under study is the solid thermal conductivity λ_s for both the synthetic and natural muds. λ_s is calculated by rearranging and solving equation (25), using the mean Θ and λ of the core sampling and thermal probe results respectively. Table 14 shows the solid thermal conductivity λ_s for the 3 tested muds, as well as the volumetric water content used in equation (25) to obtain these solid thermal conductivities. Although synthetic mud 1 and synthetic mud 2 consist of the same solid particles, different solid thermal conductivities are observed with this method. Given that λ_s is later used as input parameter to determine the VWC (Θ), it was decided an average of 3.55 W m^{-1} K^{-1} would be used consistently for further processing with synthetic mud 1 and synthetic mud 2.

	Mud type		
	Synthetic mud 1 (M1)	**Synthetic mud 2 (M2)**	**Natural mud (R)**
Solid thermal conductivity λ_s [W m^{-1} K^{-1}]	3.11	3.99	3.10
Volumetric water content Θ [m^3/m^3]	0.880	0.907	0.779

Table 14. Solid particle thermal conductivity of the synthetic mud and natural mud from the port of Rotterdam. Synthetic mud 1 and 2 share the same solid components and therefore also a common soil solid thermal conductivity λ_s.

5.3.2 DTS measurements with synthetic mud

Thermal response and interfaces for synthetic mud 1 - M1

As mentioned in Section 4.3.1, 7 out of the 9 planned tests were performed on synthetic mud 1. Tests 6 and 8 were excluded due to an error in the data transfer and henceforth did not produce plausible results. Table 6 is reprinted from Section 4.3.1 below for a reminder on the heat pulses applied and their corresponding magnitudes and durations.

Experiment code	Peak current [amps]	Duration [s]
S1-M1	1.4	150
S2-M1	1.6	150
S3-M1	1.8	150
S4-M1	1.4	300
S5-M1	1.6	300
S6-M1*	1.8	300
S7-M1	1.4	600
S8-M1*	1.6	600
S9-M1	1.8	600

*Table 6. List of heating strategies tested on a column filled with synthetic mud 1. A total of 9 experiments were planned, with currents spanning 1.4 – 1.8 amps and durations ranging from 150 to 600 seconds. *S6-M1 and S8-M1 were not processed due to errors in the data transfer procedure.*

The thermal response recorded by the FO on Pole 1 is plotted for S1-M1, S5-M1 and S9-M1 in Fig. 13, Fig. 15 and Fig. 14 below. Note that 0.0 m on the y-axis represent the position of the bottom coil on Pole 1, which is located at 0.05m above the bottom of the column. This distance was chosen to avoid any potential boundary effects interfering with the DTS recorded temperatures right at the bottom wall of the column. Keeping the geometry consistent, this entails that the first core sampling data point, which is situated at 0.05 m above the bottom of the column, corresponds to the data measured by the first FO coil on the pole (also at 0.05m). The air-water and mud-water interface are also included on the figures.

Other than the general thermal response along the pole, Fig. 13, Fig. 15 and Fig. 14 describe the interface between the media present in the column. These interfaces become increasingly more distinguishable for increasing heat pulse magnitude and duration, as the difference in their thermal properties translates itself into larger and larger temperature disparities. Air has the lowest volumetric heat capacity and therefore rapidly heats to the high temperatures observed. Water has the highest volumetric heat capacity and therefore heats slower and to a lower maximum temperature than both mud and air, whilst mud is somewhere in between. With regards to the accuracy of the interfaces, they are very close to interfaces determined from observing the set-up: air/water at 1 meter (0.95 m from the bottom FO coil as on the figures) and water/mud at 0.6 meters (0.55 m from the bottom FO coil as on the figures).

For a medium that is homogeneous and experiencing only conduction, the temperature increase by an evenly distributed heat source should be equal across the column. However, in Fig. 15 and Fig. 14, there is significant variability in the temperature distribution along 0.6 – 1.0 m of the column, likely due to the effects of convection in the water. Important to note is that S5-M1 (Fig. 15) shows residual heat in the mud section of its reference temperature (dark blue), indicating that the system had not yet cooled back down from the previous (S4-M1) test's heat pulse when it was initiated. Further processing will explain that this is something to avoid in the future, as it may affect the slope selection procedure from which thermal conductivities are derived.

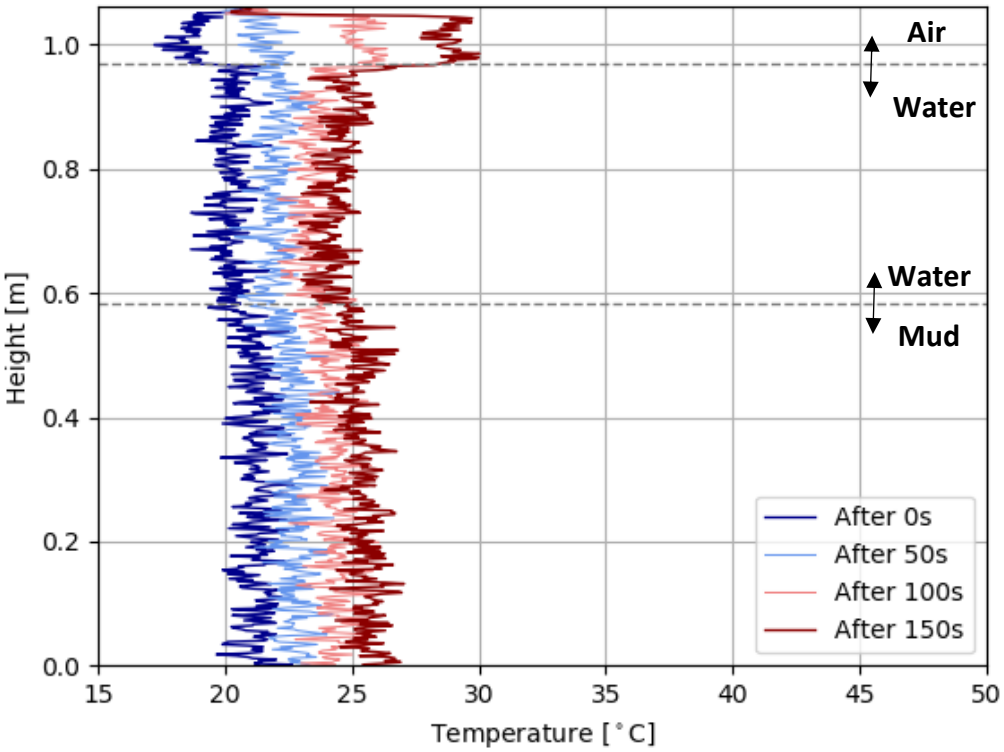

Fig. 13. S1-M1 (1.4 amps, 150s) heat pulse visualized over the vertical range of the FO cable, where 0.0 m represents the bottom coil and 1.06 m represents the top coil on Pole 1. (0.05 - 1.11 m measured from the bottom of the column).

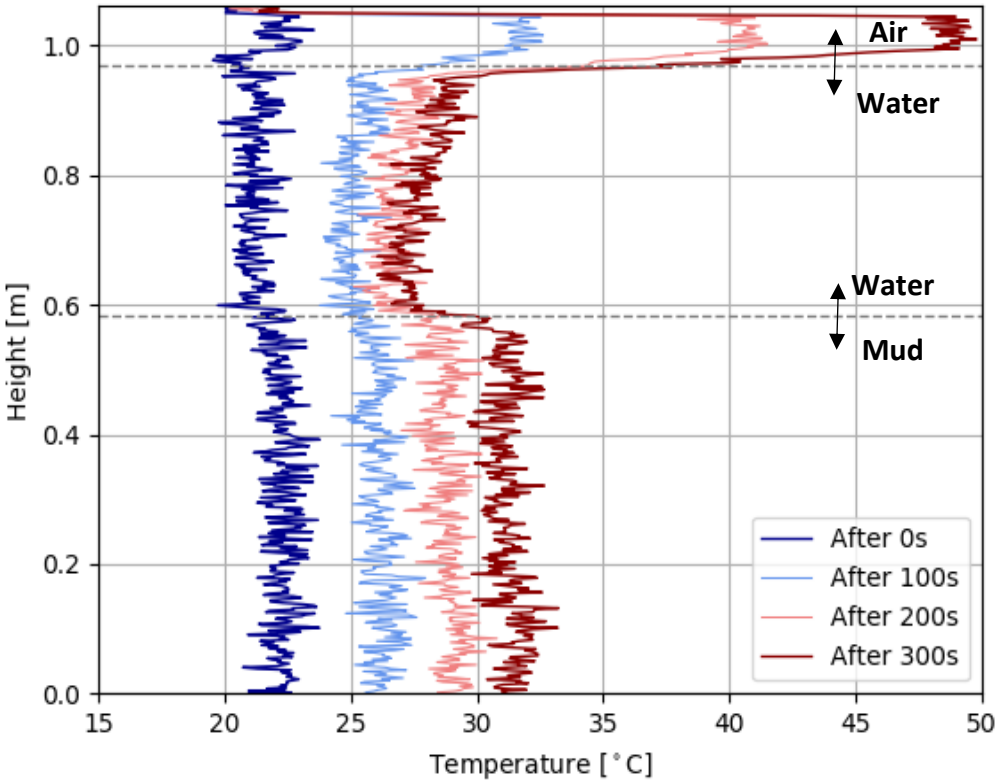

Fig. 15. S5-M1 (1.6 amps, 300s) heat pulse visualized over the vertical range of the FO cable, where 0.0 m represents the bottom coil and 1.06 m represents the top coil on Pole 1. (0.05 - 1.11 m measured from the bottom of the column).

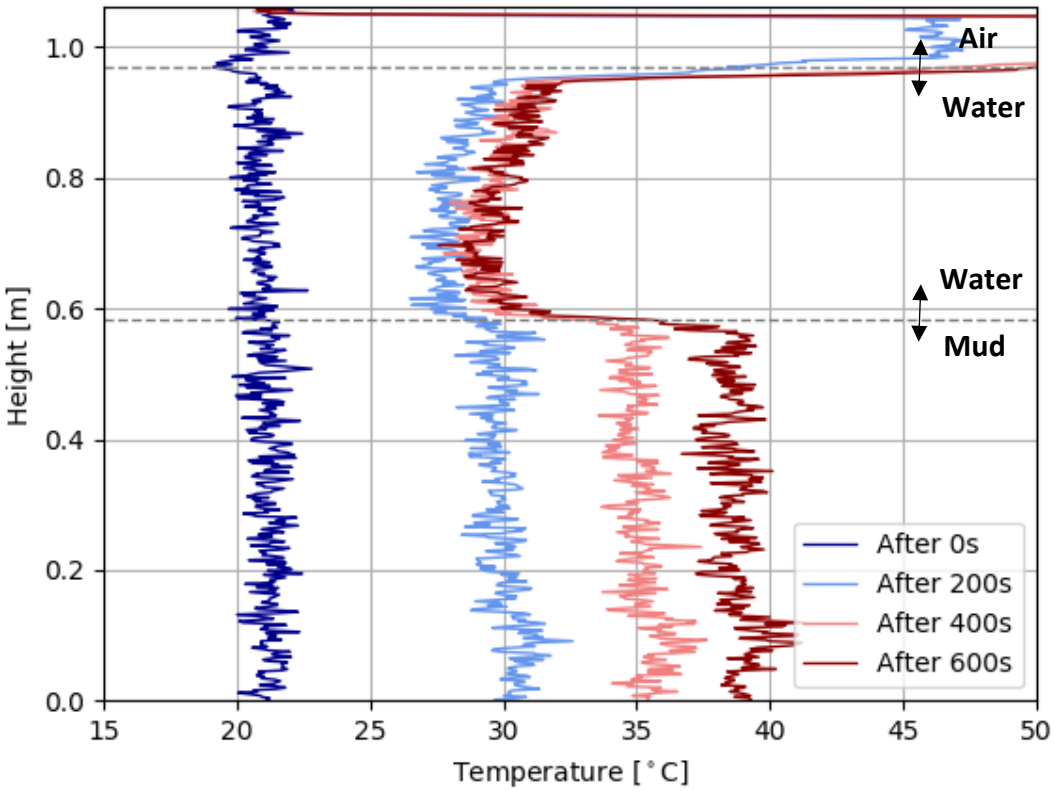

Fig. 14. S9-M1 (1.8 amps, 600s) heat pulse visualized over the vertical range of the FO cable, where 0.0 m represents the bottom coil and 1.06 m represents the top coil on Pole 1. (0.05 - 1.11 m measured from the bottom of the column).

Early cutoff time and derivation of slope

Herein, deriving the slope from the recorded thermal response will be discussed. Equation (9) dictates that a linear regression between the change in temperature ΔT and the natural logarithm of time $ln(t)$ since initiating a heat pulse will yield a slope from which the thermal conductivity can be derived. An integral component of the slope selection procedure is ensuring the section affected by the volumetric heat capacity of the set-up components and mud itself is neglected, hence a cutoff time.

The change in temperature caused by a heat pulse is found by subtracting the pre-pulse reference temperature T_0 from the DTS recorded temperature T over the duration of the heat pulse. To avoid reporting negative changes in temperature caused by local variability in DTS data right as the heat pulse is switched on, T_0 is defined as the lowest temperature recorded within 20 seconds of starting the pulse.

Fig. 16 shows the DTS recorded temperatures for all tests conducted on M1. Fig. 17 shows the resulting change in temperature when the reference temperature is subtracted from absolute temperature. The legend provided in Fig. 16 and Fig. 17 highlights the individual currents applied as well as the duration for which they were applied.

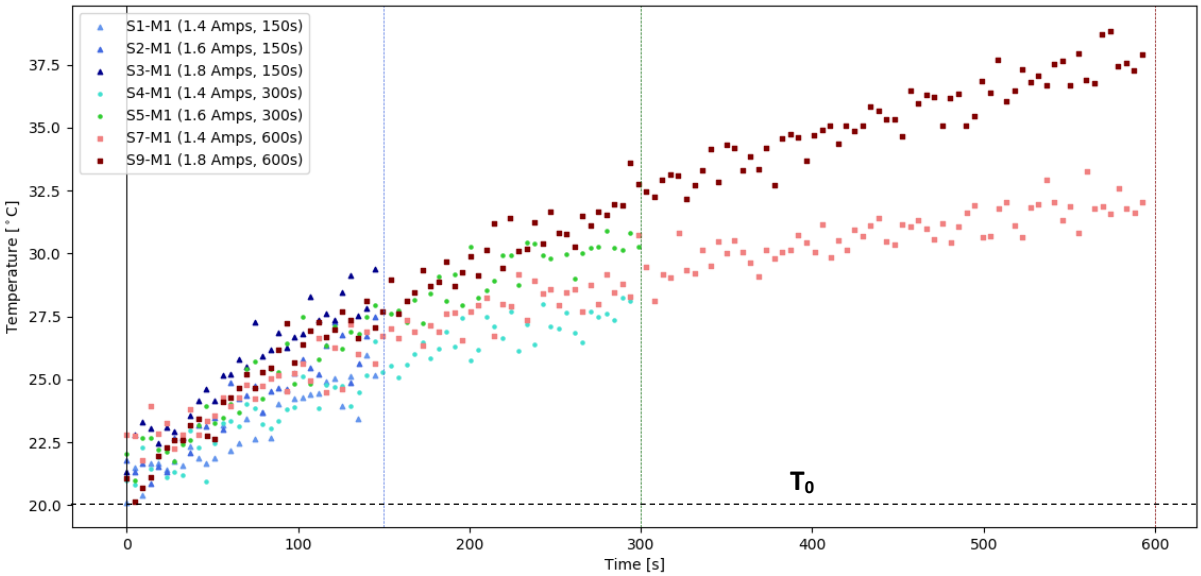

Fig. 16. Temperature measurements of the heating phase of all M1 tests. Vertical lines represent the 3 durations (150, 300 and 600 seconds). The reference temperature T_0 is also shown.

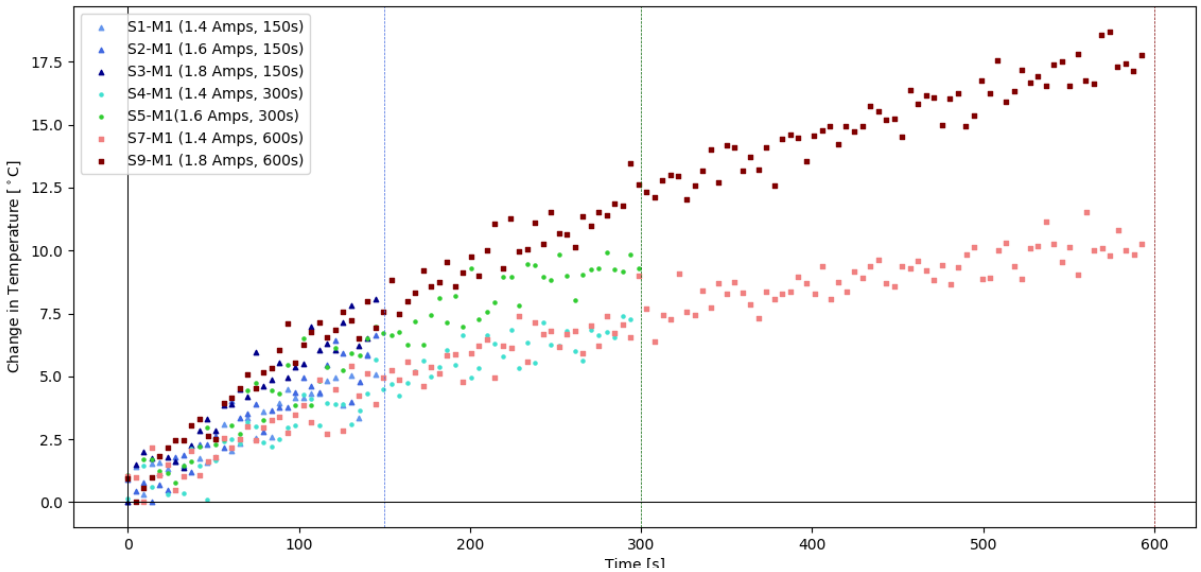

Fig. 17. Change in temperature recorded in response to all heat pulses tested on M1. Vertical lines represent the 3 durations (150, 300 and 600 seconds).

Fig. 17 reveals that tests conducted with the same applied current follow a similar 'change in temperature' curve for their overlapping durations, irrespective of their total duration. This insinuates there is a certain degree of repeatability to the procedure, allowing for a more thorough investigation.

The following step in the process is to perform a linear regression on the $\Delta T - \ln(t)$ plots for all DTS tests performed. The result is a line of best fit, with a slope characterized by the thermal conductivity of the heated medium. However, to ensure the approximation detailed in equation (9) is valid, a certain time correction factor must be included in the analysis. With the time correction factor not known a priori, an equally valid approach is to omit a certain amount of early time data from the linear regression. Sources argue that errors in the approximation suggested by equation (9) at early time data are concentrated in the first 5 – 10 seconds of the heat pulse (Bristow et al., 1994), whilst others suggest that the error is significant even after 120 seconds of heating (Ciocca et al., 2012). To overcome the lack of consesus on an acceptable early time cutoff, this research presents a method through which the cutoff time is decided individually per experiment.

The early time cutoff marks the change in slope of a $\Delta T - \ln(t)$ plot where the thermal response is no longer influenced by the volumetric heat capacity of the set-up and thermal conductivity effects are henceforth expected to dominate. This slope will ultimately be used to derive the thermal conductivity of the soil, as per equation (9). The aforementioned change in slope is practically observed as the "knee" of a $\Delta T - \ln(t)$ plot. Fig. 18, Fig. 19 and Fig. 20 are the $\Delta T - \ln(t)$ plots for S3-M1, S5-M1 and S9-M1 selected for visualization of the process.To ensure a robust cutoff time selection, the $\Delta T - \ln(t)$ progression of 3 slices along the column are plotted on the same graph, one 0.05 m from the top of the mud column, one in the center and one 0.05 m from the bottom of the mud column.

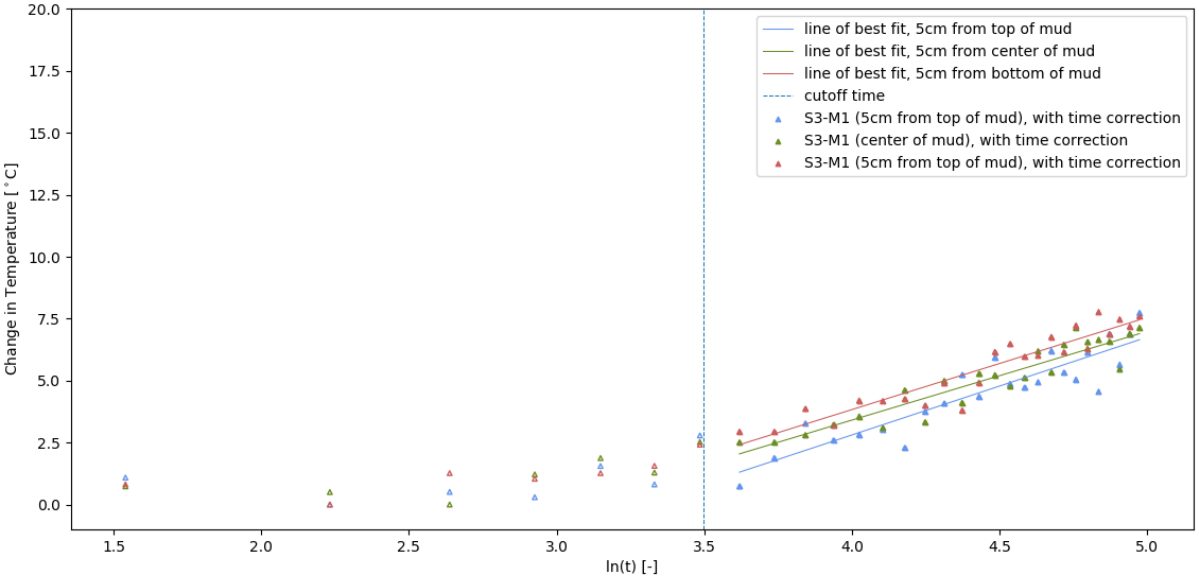

Fig. 18. Change in temperature recorded during S3-M1 (1.8 amps, 150s) vs the natural logarithm of time since the initiation of the heat pulse. The dotted vertical line represents the cutoff time that separates data used for slope processing from the conventionally discarded early time data. The cutoff time is selected based on DTS temperatures recorded near the top, center and bottom of the mud column.

The dotted vertical line represents the early cutoff time that separates data used for slope processing from the conventionally discarded early time data. It may be observed that the position of the "knee" is variable across experiments, so care should be taken to individually analyse all tests.

An important observation from Fig. 18, Fig. 19 and Fig. 20 is that, based on the current procedure, the cutoff time becomes larger for tests of increasing duration (150 vs 300 vs 600 seconds). In theory, the duration of the heat pulse should not have an impact on the time it takes to transition between the region influenced by the volumetric heat capacity of the set-up to where thermal conductivity effects are expected to dominate. This result insinuates that the current early time cutoff procedure is not yet optimized. A modified approach is proposed in a later section of the report, titled "*Late cut off time and derivation of slope*".

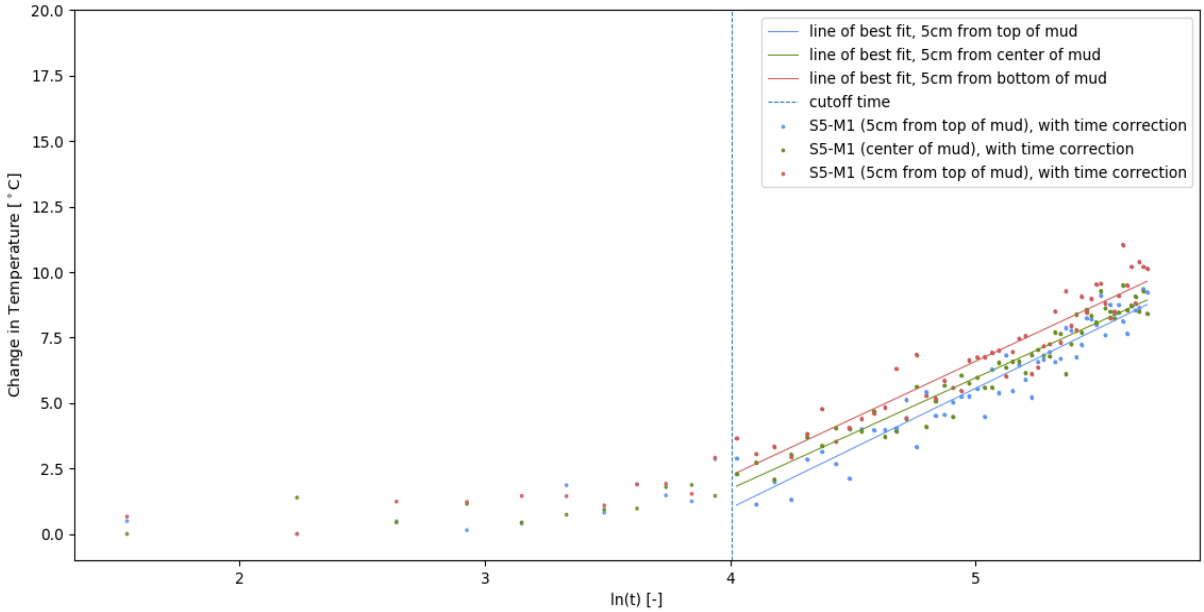

Fig. 19. Change in temperature recorded during S5-M1 (1.6 amps, 300s) vs the natural logarithm of time since the initiation of the heat pulse. The dotted vertical line represents the cutoff time that separates data used for slope processing from the conventionally discarded early time data. The cutoff time is selected based on DTS temperatures recorded near the top, center and bottom of the mud column.

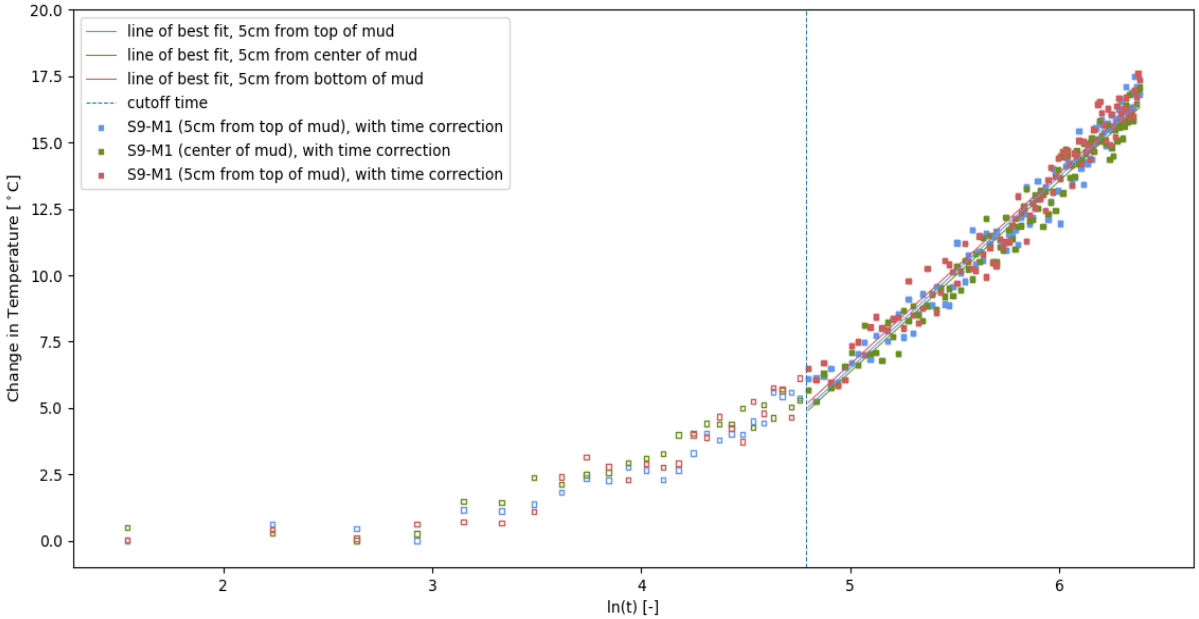

Fig. 20. Change in temperature recorded during S9-M1 (1.8 amps, 600s) vs the natural logarithm of time since the initiation of the heat pulse. The dotted vertical line represents the cutoff time that separates data used for slope processing from the conventionally discarded early time data. The cutoff time is selected based on DTS temperatures recorded near the top, center and bottom of the mud column.

It is found that the slopes produced from the linear regressions of all tests yield significantly varying results, even for experiments with the same supplied current where similar slopes are expected (see Table 15). Table 15 groups the tests performed by current supplied (1.4, 1.6 and 1.8 amps) to highlight the difference in slopes obtained, as shown by the procedure described in the previous section. Shorter experiments (150 s) in particular feature smaller slopes and larger standard deviations. The increased spread in the data of S1-M1, S2-M1 and S3-M1 is undoubtedly the result of the lower S/N ratio obtained from the smaller heat pulses.

	S1-M1	**S4-M1**	**S7-M1**	**S2-M1**	**S5-M1**	**S8-M1**	**S3-M1**	**S6-M1**	**S9-M1**
Peak current [Amps]	1.4			1.6			1.8		
Duration [s]	150	300	600	150	300	600	150	300	600
Date of experiment	18/06	19/06	19/06	18/06	19/06	/	18/06	/	23/06
Experiment order (daily)	1	1	3	2	2	/	3	/	1
Average slope along depth profile [°C]	2.48	3.26	3.84	3.11	4.25	/	3.83	/	7.33
Standard deviation [°C]	0.326	0.210	0.125	0.329	0.199	/	0.320	/	0.183

Table 15. Slopes determined from the ΔT vs ln(t) relationship of tests S1-M1 through to S9-M1, along with the associated standard deviation and date of recording. S6-M1 and S8-M1 were not processed due to errors in the data transfer procedure.

Based on these findings, also visualized in Fig. 21, it was decided that any subsequent processing would omit test results from pulses with a duration of 150 seconds (S1-M1, S2-M1 and S3-M1) due to the excessive spread in slopes that would likely translate to an unacceptably large spread in VWC (Θ) as well.

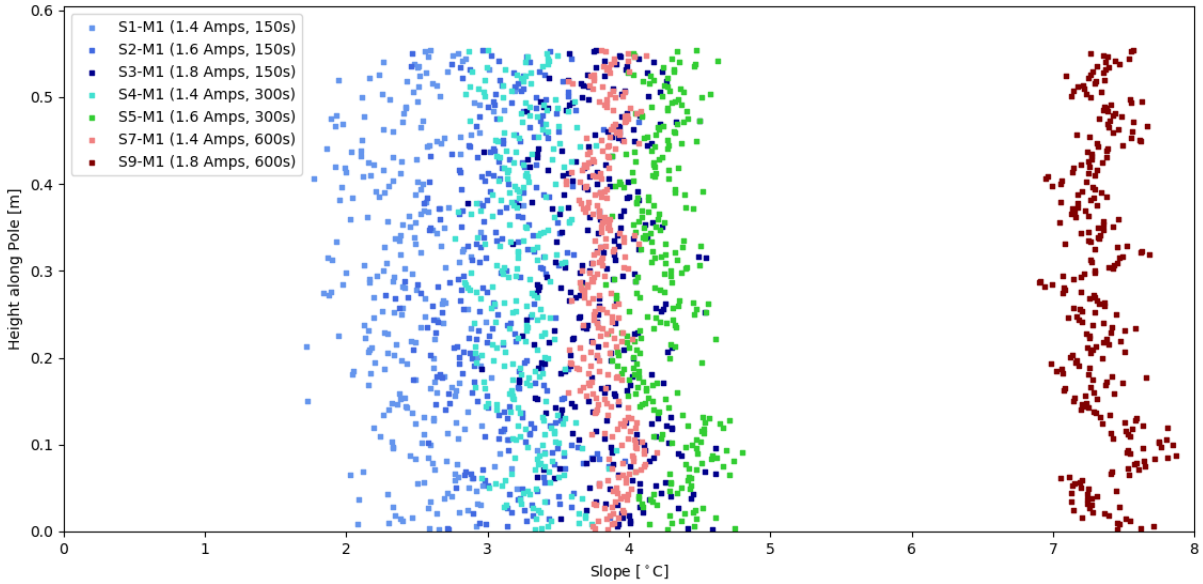

Fig. 21. Slopes determined from the ΔT vs ln(t) relationship of tests S1-M1 through to S9-M1.

Translating slopes to water content

Translating slopes to water content occurs by means of the following steps:

$$\lambda = \frac{q}{slope} \tag{28}$$

where q is the heat flux in W m^{-1} and the '*slope'* comes from the fitted linear regression lines obtained by means described in the previous section. Determining the heat flux applied to the system depends on the properties of the heating cable, the geometry and the current applied. Thusfar, reported currents have been the peak currents obtained from the (AC) power supply unit. To calculate the power dissipated as heat to the system, this peak current I_{pk} must first be converted to an rms current I_{rms}.

$I_{rms} = \frac{I_{pk}}{\sqrt{2}}$, for a sinusoidal signal with 0 offset. (29)

The average power P [W] is then given by the product of the total heating wire resistance R [Ω] and the squared rms current I_{rms}.

$$P = R * {I_{rms}}^2 \tag{30}$$

The heat flux for an uncoiled section of cable is then calculated by dividing the average power by the total length *L* [m] of the cable. However, the coiled geometry of the heating wire must also be taken into account. With a coil density of 300 coils per vertical meter of pole and a single coil length of approximately 0.12 m, every vertical meter of the column contains 36 m of heating cable. The effective heat flux is therefore given by equation (31)

$$q = \frac{R*{I_{rms}}^2}{L} * 36 \tag{31}$$

The thermal conductivity λ is then converted into VWC (Θ) by equation (26):

$\theta = \frac{\ln\left(\lambda/\lambda_s\right)}{\ln\left(\lambda_w/\lambda_s\right)}$, with λ_s and λ_w now known.

For a total cable length and resistance of 38 m and 60.4 Ω respectively, and all other input parameters known, the VWC (Θ) along the height of the mud column for tests S4-M1 through to S9-M1 can be calculated and displayed as in Table 16 and

Fig. 22.

When plotted vs the VWC (Θ) (

Fig. 22) obtained from core sampling, 3 observations can be made:

(I) Heat pulses S4/5, S7 and S9 yield largely different VWC's (Θ) whilst all being conducted on the same mud. Furthermore, core sampling results predict a consistent water content along the depth;

(II) Tests S4 and S5 yield similar VWC's (Θ) even though they have a varying heat pulse magnitude;

(III) There is an offset in the VWC's (Θ) determined from DTS data compared to VWC's (Θ) obtained from core sampling. (0.601 m^3m^{-3} vs 0.879 m^3m^{-3} on average).

	S4-M1	S7-M1	S5-M1	S8-M1*	S6-M1*	S9-M1
Peak current [Amps]	1.4		1.6		1.8	
Duration [s]	300	600	300	/	/	600
Date of experiment	19/06	19/06	19/06	/	/	23/06
Experiment order (daily)	1	3	2	/	/	1
Average thermal conductivity [$Wm^{-1}K^{-1}$]	1.37	1.16	1.37	/	/	1.00
Average VWC (Θ) along depth profile [$m^3\,m^{-3}$]	0.535	0.627	0.534	/	/	0.708
Standard deviation [$m^3\,m^{-3}$]	0.036	0.018	0.026	/	/	0.014

*grouped by peak current magnitude supplied. *S6-M1 and S8-M1 were not processed due to errors in the data transfer procedure.*

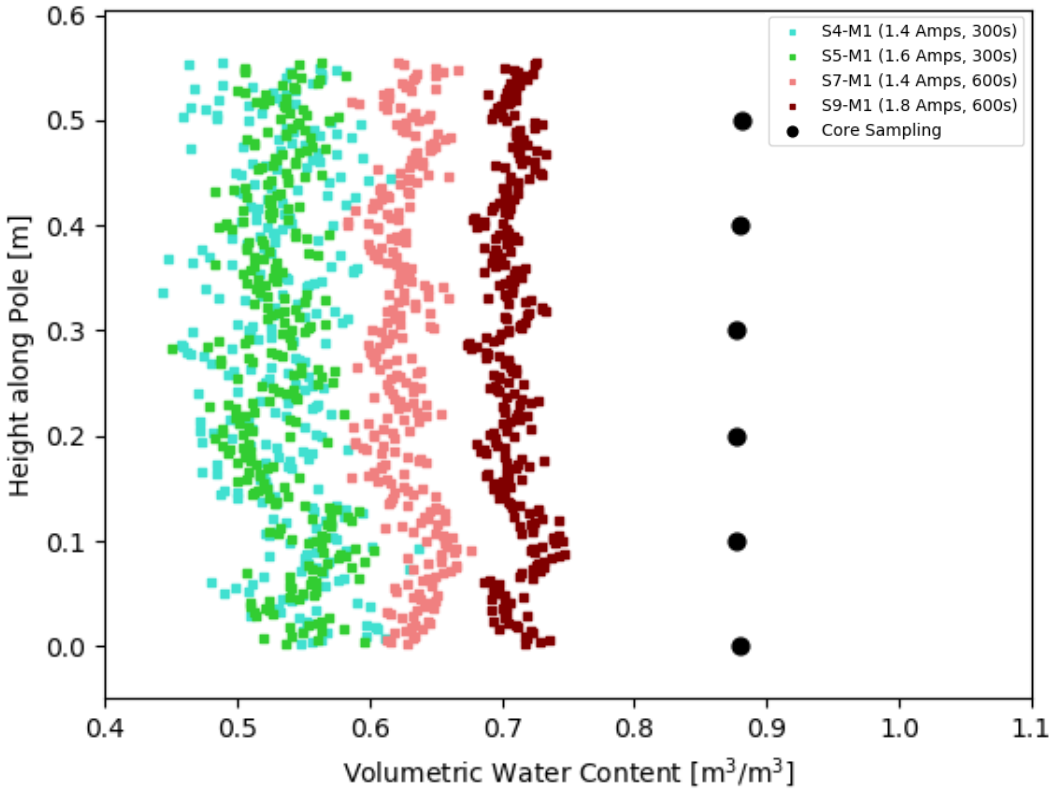

Fig. 22. VWC (Θ) determined using core sampling (black circles) and DTS data from S4-M1 through to S9-M1

Late cut off time and derivation of slope

Observation (I) indicates that the slope selection procedure described earlier is not yet optimized and does not produce the correct VWC's (*Θ*). However, observation (II) suggests that the slope selection procedure for tests with a duration of 300 seconds produces repeatable results in VWC (*Θ*) irrespective of current supplied. In response to these findings, a modification to the original method is therefore proposed.

Based on the desirable results obtained from experiments S4-M1 and S5-M1 as stated in observation (II), it was decided to introduce a late time cutoff to all experiments exceeding 300 seconds in duration. The hypothesis was that a 300 s late-time cutoff applied to experiments of longer duration (600s) would result in coherent VWC's (*Θ*) similar to those observed in S4-M1 and S5-M1. If we then revisit the $\Delta T - \ln(t)$ plots of the tests with a longer heat pulse duration (600 seconds), it can be observed that the curve can be split into three distinct sections, each with their own slope. Fig. 23 is a sample curve used to visualize the three sections. If this hypothesis proves to be true, it may be stated that the section of the curve producing the most robust slopes to process into VWC's (*Θ*) is bounded by an early cutoff time dependent on the individual experiment, and a late cutoff time of 300 seconds.

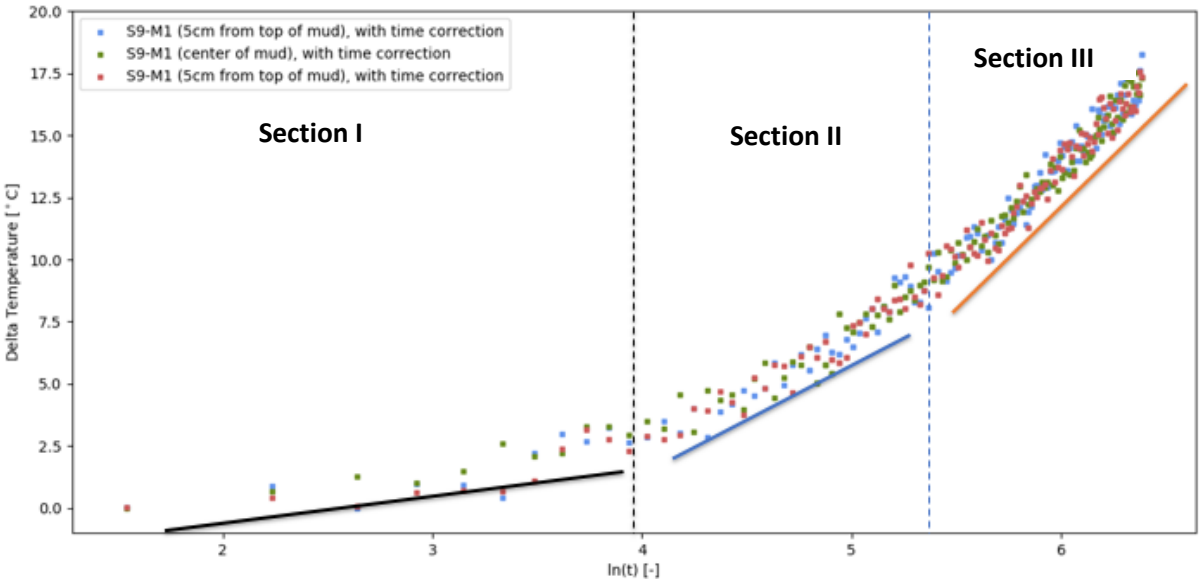

Fig. 23. The ΔT vs ln(t) plot on a semi-log scale can be divided into three distinct sections with increasing slopes. The slope of the linear regression between ΔT and ln(t) is used to determine thermal conductivity and ultimately VWC (Θ). It is therefore important to select the section of the curve where thermal conductivity effects are expected to dominate.

The underlying cause of the increase in slope shown in Section III of Fig. 23 is not so easily rationalized. A possible explanation may be that the muds tested are sufficiently diluted such that convective cells form in the test column after a certain period of heating. When the convective term becomes large enough, the thermal response is no longer solely characterized by Fourier's law of heat conduction and thus the approximation used to derive λ may fail.

Putting theory into practice, the slopes of experiments S7-M1 and S9-M1 were recomputed with late-time cutoff at 300 seconds and printed in Table 17. Grouping by peak current magnitude, it is observed that the computed slopes are now very much in agreement between S4-M1 and S7-M1. Unfortunately, due to the loss of data for S6-M1 and S8-M1, no comparison can be made in slopes for

peak currents of 1.6 amps and 1.8 amps. However, once all slopes are translated to VWC (Θ), all DTS tests produce results in the same range, justifying the implementation of the modified approach.

Fig. 24 is the representation of VWC's (Θ) calculated from DTS data using the modified approach with cutoffs at 55 seconds and 300 seconds, prior to spatial averaging. Although the DTS results are now in agreement, the offset first described in observation (III) between DTS data and core sampling data (black circles) still remains and will be investigated in the following section.

	S4-M1	S7-M1	S5-M1	S8-M1*	S6-M1*	S9-M1
Peak current [Amps]	1.4		1.6		1.8	
Duration [s]	300	Cutoff at 300	300	/	/	Cutoff at 300
Date of experiment	19/06	19/06	19/06	/	/	23/06
Experiment order (daily)	1	3	2	/	/	1
Average slope along depth profile [°C]	3.26	3.17	4.25	/	/	5.23
Standard deviation [°C]	0.210	0.187	0.199	/	/	0.207

Table 17. Slopes obtained from the ΔT vs ln(t) plot for tests S4-M1 through to S9-M1, grouped by peak current magnitude. Tests S6-S9 were cut at 300s so that only the mid-section of the curve was used for slope calculations. (see Fig. 23 for a visualization of the described mid-section).

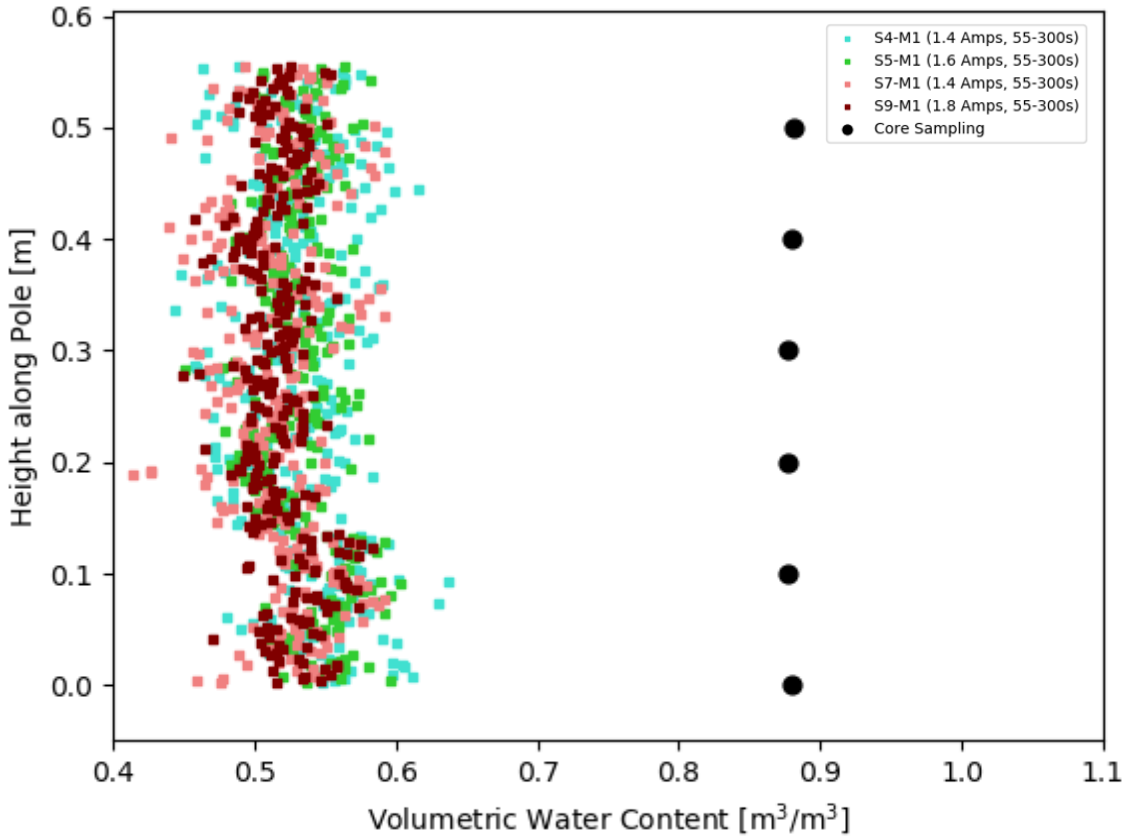

Fig. 24. Volumetric water content determined using core sampling (black circles) and DTS data from S4-M1 through to S9-M1, with cutoffs at 55s and 300s (prior to spatial averaging).

Offset correction

Given that the offset in observation (III) is approximately, constant for all tests, it is likely the result of an over or underestimation in one of the inputs used to translate between thermal conductivity and volumetric water content (equation (26)) i.e.: mud thermal conductivity λ, mud solid thermal conductivity λ_s or water thermal conductivity λ_w. Given that λ_s was obtained by direct conventional testing and λ_w from reference by literature (Lu et al., 2007), the uncertainty likely originates from the mud thermal conductivity λ obtained from equation (26). The DTS estimated thermal conductivity, seen in Table 18, is between 1.37 and 1.41 W m^{-1} K^{-1}, whereas the thermal conductivity obtained with the conventional thermal probe for this mud yields a λ of 0.75 W m^{-1} K^{-1}. Assuming that the modified slope selection procedure is now robust, the error must therefore originate from the effective heat flux parameter *q* in equation (28).

Thus far, *q* was determined based on the resistance of the total wire, the rms current applied and the geometry of the set-up (coiling). However, *q* may also be back-calculated from equations (9) and (25), assuming accurate reference values for VWC (Θ), λ_w and λ_s can be supplied. These parameters have indeed already been determined by direct measurements (see section 5.3.1), and thus we use the following rearrangement of equations to back calculate a predicted heat flux:

1) $\lambda = {\lambda_s}^{1-\theta}{\lambda_w}^{\theta}$, where θ is the average VWC (θ) obtained from core sampling

2) $q = slope * \lambda$, where λ is taken from 1) and the slope is obtained from the linear regression of $\Delta T - \ln(t)$ with the modified approach (late-time cutoff at 300 s).

The results for calculated and backwards-calculated (predicted) heat fluxes are printed in Table 18 below, along with the corresponding thermal conductivities. It is evident that the predicted heat fluxes and subsequent thermal conductivities are smaller by an average factor of 1.87 across all experiments. Therefore, there must be a set-up related complicating factor that causes the actual heat flux delivered to the system to be diminished/delayed.

	S4-M1	**S7-M1**	**S5-M1**	**S8-M1**	**S6-M1**	**S9-M1**
Peak current [Amps]	1.4		1.6		1.8	
Calculated heat flux [W m^{-1}]	55.8		72.9		92.2	
Duration [s]	300	Cutoff at 300	300	/	/	Cutoff at 300
Predicted heat flux [W m^{-1}]	30.2	29.4	39.4	/	/	48.5
Calculated thermal conductivity [W m^{-1} K^{-1}]	1.37	1.41	1.37	/	/	1.40
Predicted thermal conductivity [W m^{-1} K^{-1}]	0.73	0.75	0.73	/	/	0.75
Correction factor	1.85	1.90	1.85	/	/	1.90

Table 18. A comparison of the heat flux calculated from the geometry and peak current applied to the set-up vs the heat flux predicted from back-calculation with the core sampling VWC (Θ) in equation (25) and the linear regression of equation (9). Subsequently, calculated and predicted thermal conductivities are also shown, as well as the factor difference between them (correction factor). For reference, the thermal conductivity of M1 obtained by thermal needle probe was 0.75 Wm^{-1}K^{-1}.

Cause(s) for offset in heat flux

Thus far, the thermal conductivity of the set-up has been assumed negligible, such that a heat flux produced in the heating wire is directly transferred into the surrounding mud. However, with the results presented in Table 19 above, it may be that this approximation is the cause of the correction factor in q.

Fig. 25 is a horizontal cross section of the system filled with mud, highlighting a layered structure that the heat must pass through before it reaches the mud. The heat is assumed to dissipate radially, and any heat loss through the foam-filled PVC pole is assumed to be negligible. To get an idea of the impact of the set-up materials on the heat flux, it is worth focusing on the 1D representation displayed in Fig. 26.

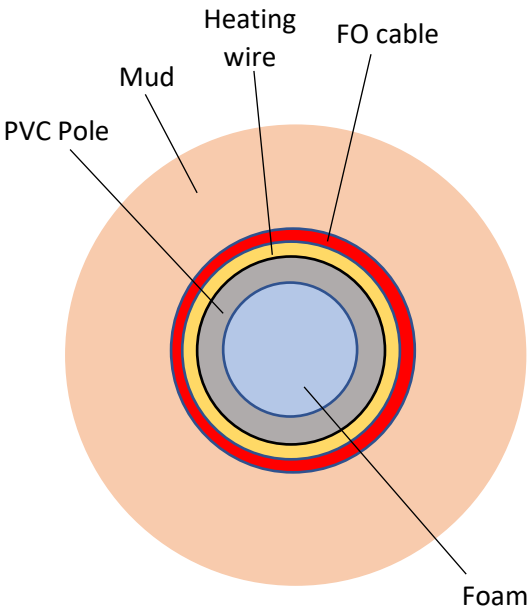

Fig. 25. A horizontal slice through the experimental set-up. The water-filled PVC pole is coiled by a silicone-sheathed heating wire, which is in turn coiled by a FO cable. Heat is assumed to dissipate radially outward from the heating wire.

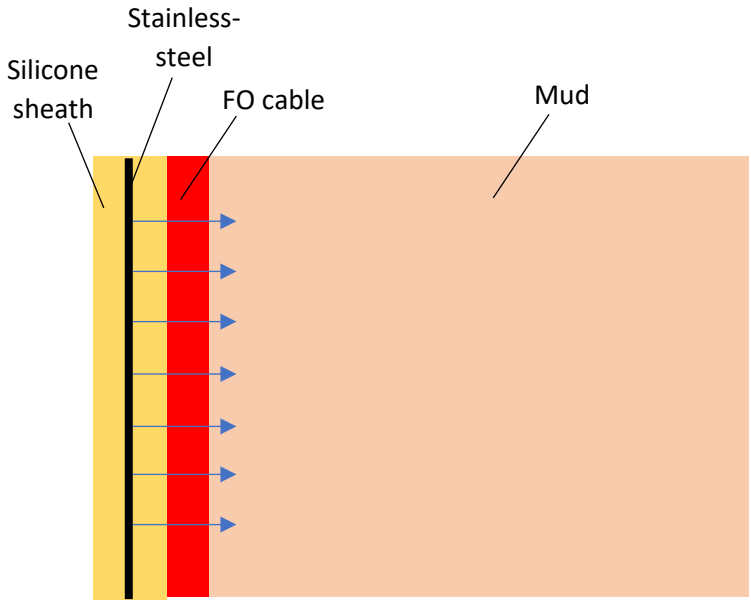

Fig. 26. 1D representation of the set-up. Blue arrows represent the direction of heat, flowing from the stainless-steel core, through the silicone sheath, through the FO cable and into the mud.

The thermal conductivity of the set-up may be calculated by considering the thermal conductivities of the individual components in series. Thermal resistances R are additive when occurring in series and given by the formulas:

$$R_n = \frac{L_n}{\lambda_n * A} \tag{32}$$

And

$$R_T = \frac{1}{R_1} + \frac{1}{R_2} + \frac{1}{R_3} + \cdots \quad (33)$$

where L is the thickness of the section traversed by the heat flux, λ is the thermal conductivity of the individual set-up component and A is the area perpendicular to the heat flux and R_T is the total thermal resistance [K W^{-1}]. The thermal conductivities and thicknesses of the set-up components are given in Section 3.3.4 (Table 2), and the area the heat flux passes through is the found by multiplying the circumference of the cylinder circumscribed by the heating wire (2*π*0.019) with the vertical length of this same cylinder (1.06 meters). The equivalent thermal conductivity of the materials in series is found by then rearranging equation (32) for λ and taking L_n as the total set-up thickness. For this set-up, the equivalent thermal conductivity was thus determined to be 0.111 W m^{-1} K^{-1}. This is significantly lower than the thermal conductivity of the mud and is expected to act as a sort of insulator, reducing the effective heat flux on the mud.

Whilst the insulating properties of some of these components would indeed affect the heat flux in the direction observed (diminishingly), a quantitative analysis is required to provide conclusive evidence on the matter. Other potential factors that could be contributing to the discrepancy are heat loss in the axial direction, imperfect contact resistances, etc.

Volumetric water content after correction for q

Proceeding with the correction factor (1.87) applied to the calculated heat flux, new VWC's (Θ) were computed and their average compared to that of the VWC's (Θ) obtained from core sampling (see Table 19).

	S4-M1	S7-M1	S5-M1	S8-M1	S6-M1	S9-M1		
Peak current [Amps]	1.4		1.6		1.8			
Duration [s]	300	Cutoff at 300	300	Cutoff at 300	300	Cutoff at 300		
Date of experiment	19/06	19/06	19/06	/	/	23/06		
Experiment order (daily)	1	3	2	/	/	1	**Average VWC (Θ) across experiments [m^3 m^{-3}]**	**Core sampling average VWC (Θ) [m^3 m^{-3}]**
Average VWC (Θ) along depth profile [m^3 m^{-3}]	0.886	0.870	0.885	/	/	0.870	0.878	0.879
Standard deviation [m^3 m^{-3}]	0.036	0.033	0.026	/	/	0.022	0.029	0.001

Table 19. VWC (Θ) obtained by down-scaling the calculated heat flux by the average correction factor obtained from synthetic mud 1 and 2 (mean correction factor = 1.87). Average VWC (Θ) determined by core sampling is also printed for comparison.

The modified slope selection method and corrected heat flux appear to produce VWC's (Θ) that are, on average, very close to those determined from core sampling (0.878 vs 0.879 respectively). However, the standard deviation is significantly higher (0.029 vs 0.001). This spread in the results of S4-M1 through to S9-M1 is visualized in Fig. 27 below. By applying a Savitzky-Golay filter (scipy in python) to the DTS VWC's (Θ), the results are spatially averaged and yield a line of best fit more closely resembling the core sampling results (see Fig. 28). This filter produces a polynomial fit to 2n+1

neighboring point including the point to be smoothed. It handles like a weighted moving average in that all coefficients are the same for every ‘y’ value in the dataset.

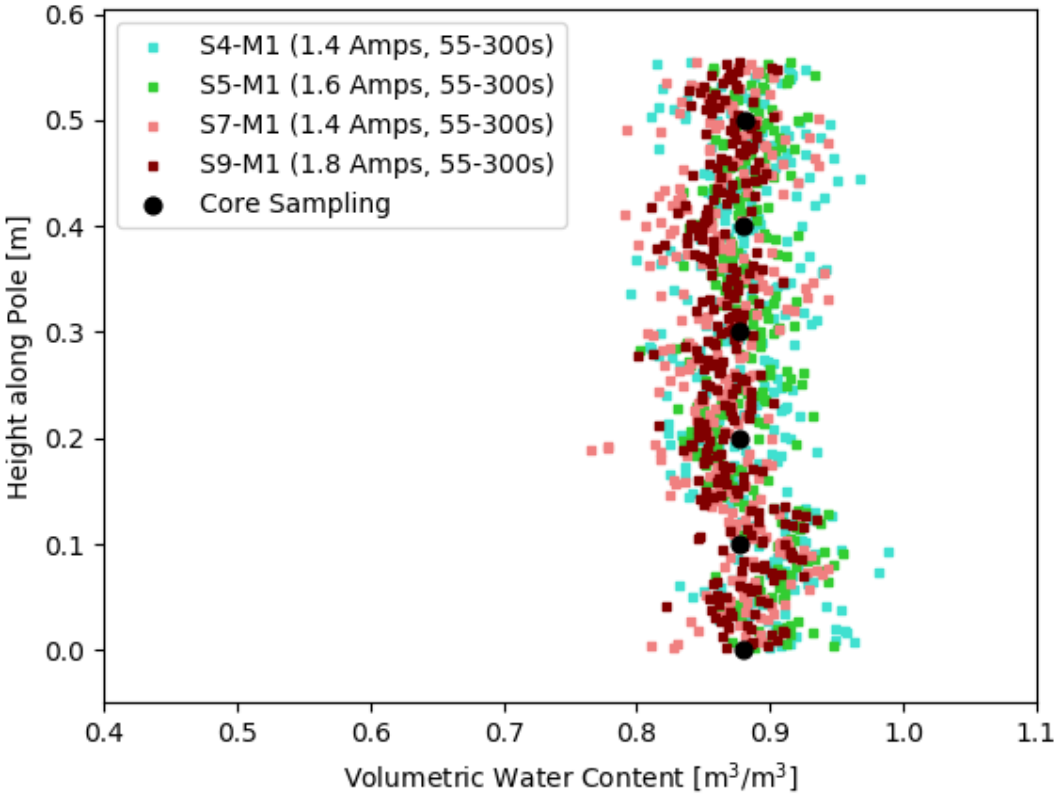

Fig. 27. Volumetric water content for DTS data determined by down-scaling the heat flux with a correction factor of 1.87. DTS data from S4-M1 through to S9-M1 is displayed, with cutoff times at 55 s and 300 s. VWC (Θ) obtained from core sampling is also visualized (black circles). Cutoffs used were 55 s and 300 s.

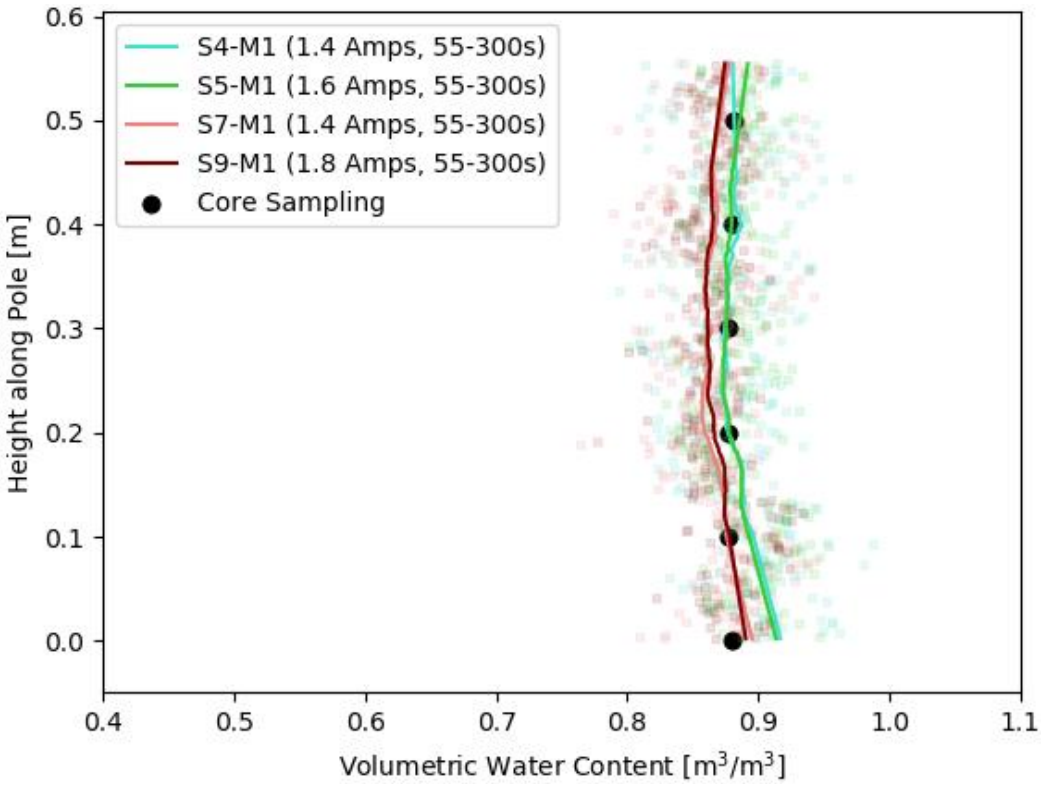

Fig. 28. Smoothed VWC (Θ) results using a Savitzky-Golay filter for tests S4-M1 through to S9-M1. Spatially averaged results reduce the spread in the original VWC (Θ) data obtained from DTS results.

From Fig. 28, it isn't directly obvious what heating strategy produces the best VWC (Θ) results.

Deriving water content from DTS data using the developed approach.

To verify its robustness, the data processing approach developed from synthetic mud 1 data in the previous section must now also be applied to synthetic mud 2. This section will present the outcome of the slope selection procedure, as well as the correction of the heat flux *q*.

Table 20 highlights that for experiments of equal (peak) current magnitude performed in synthetic mud 2, the slopes obtained are in very good agreement with one another.

	S4-M2	S7-M2 (300s)	S5-M2	S8-M2 (300s)	S6-M2	S9-M2 (300s)
Peak current [Amps]	1.4		1.6		1.8	
Date of experiment	01/07	02/07	01/07	02/07	01/07	02/07
Experiment order (daily)	1	1	2	2	3	3
Average slope along depth profile [°C]	3.54	3.55	4.26	4.44	5.42	5.56
Standard deviation [°C]	0.192	0.250	0.292	0.329	0.340	0.327

Table 20. Slopes obtained from the ΔT vs ln(t) plot for tests S4-M2 through to S9-M2, grouped by peak current magnitude. Tests S6-S9 were cut at 300s so that only the mid-section of the curve was used for slope calculations.

From Table 21, it may be observed that calculated and predicted thermal conductivities are lower for synthetic mud 2 than for synthetic mud 1. This is expected, since synthetic mud 2 has both a larger water content and smaller soil solid content. Strikingly, the correction factor for this mud is, on average, also 1.87. The predicted thermal conductivity, obtained from back-calculating is 0.70 W m^{-1} K^{-1}, very close to the value obtained from the thermal probe (0.69 W m^{-1} K^{-1}).

	S4-M2	S7-M2	S5-M2	S8-M2	S6-M2	S9-M2
Peak current [Amps]	1.4		1.6		1.8	
Calculated heat flux [W m^{-1}]	55.8		72.9		92.2	
Duration [s]	300	Cutoff at 300	300	Cutoff at 300	300	Cutoff at 300
Predicted heat flux* [W m^{-1}]	31.1	31.2	37.5	39.1	47.7	48.9
Calculated thermal conductivity [W m^{-1} K^{-1}]	1.26	1.26	1.37	1.31	1.36	1.32
Predicted thermal conductivity [W m^{-1} K^{-1}]	0.67	0.67	0.73	0.70	0.73	0.71
Correction factor	1.79	1.79	1.94	1.87	1.93	1.88

Table 21. A comparison of the heat flux calculated from the geometry and peak current applied to the set-up vs the heat flux predicted from back-calculation with the core sampling VWC (Θ) in equation (25) and the linear regression of equation (9). Subsequently, calculated and predicted thermal conductivities are also shown, as well as the factor difference between them (correction factor). For reference, the thermal conductivity of M1 obtained by thermal needle probe was 0.69 W m^{-1} K^{-1}.

	S4-M2	S7-M2	S5-M2	S8-M2	S6-M2	S9-M2		
Peak current [Amps]	1.4		1.6		1.8			
Duration [s]	300	Cutoff at 300	300	Cutoff at 300	300	Cutoff at 300		
Date of experiment	01/07	02/07	01/07	02/07	01/07	02/07		
Experiment order (daily)	1	1	2	2	3	3	**Average VWC (Θ) across experiments [$m^3\ m^{-3}$]**	**Core sampling average VWC (Θ) [$m^3\ m^{-3}$]**
Average VWC (Θ) along depth profile [$m^3\ m^{-3}$]	0.931	0.932	0.885	0.908	0.888	0.903	0.908	0.908
Standard deviation [$m^3\ m^{-3}$]	0.031	0.040	0.039	0.042	0.036	0.033	0.037	0.002

Table 22. VWC (Θ) obtained by down-scaling the calculated heat flux by the average correction factor obtained from synthetic mud 1 and 2 (mean correction factor = 1.87). Average VWC (Θ) determined by core sampling is also printed for comparison.

Upon correction of the heat flux, the average VWC (Θ) along the depth profiles of every test is computed and ultimately compared to the core sampling average VWC (Θ) in Table 22. It may be observed that averaging the results of all tests yields a better VWC (Θ) approximation than any single test on its own. The data presented in Table 22 is illustrated, in similar fashion to synthetic mud 1, in Fig. 29 and Fig. 30 below (with and without Savitzky-Golay filter).

Notably, the cutoff for the early time data of tests S4-M2 and S7-M2 were both at 45 seconds, whilst all other tests were cut at 70 seconds. The reason for this deviation is that both S4 and S7 were performed as the first tests of the day, and therefore had no residual heat from a previous pulse in the mud column when they started. Tests S5, S6, S8 and S9 were performed with insufficient cooling time between them, so that the heat induced from the preceding experiments had not yet dissipated. In the early time cutoff selection procedure, this translates to a later cutoff (70 s vs 45 s).

The VWC's (Θ) determined from synthetic mud 2 are, on average, very close to those determined from core sampling (0.908 vs 0.908 respectively). However, the standard deviation is significantly higher (0.037 vs 0.002). Both these observations closely resemble the outcome of the data processing of synthetic mud 1.

However, unlike the tests performed on synthetic mud 1, Fig. 30 illustrates how individual tests S8-M2 and S9-M2 produce the most accurate results (0.908 and 0.903 vs 0.908 from core sampling. Although inconclusive, this would suggest that larger heat pulse magnitudes (1.6, 1.8 amps) of longer durations (600 s) are potentially superior heating strategies.

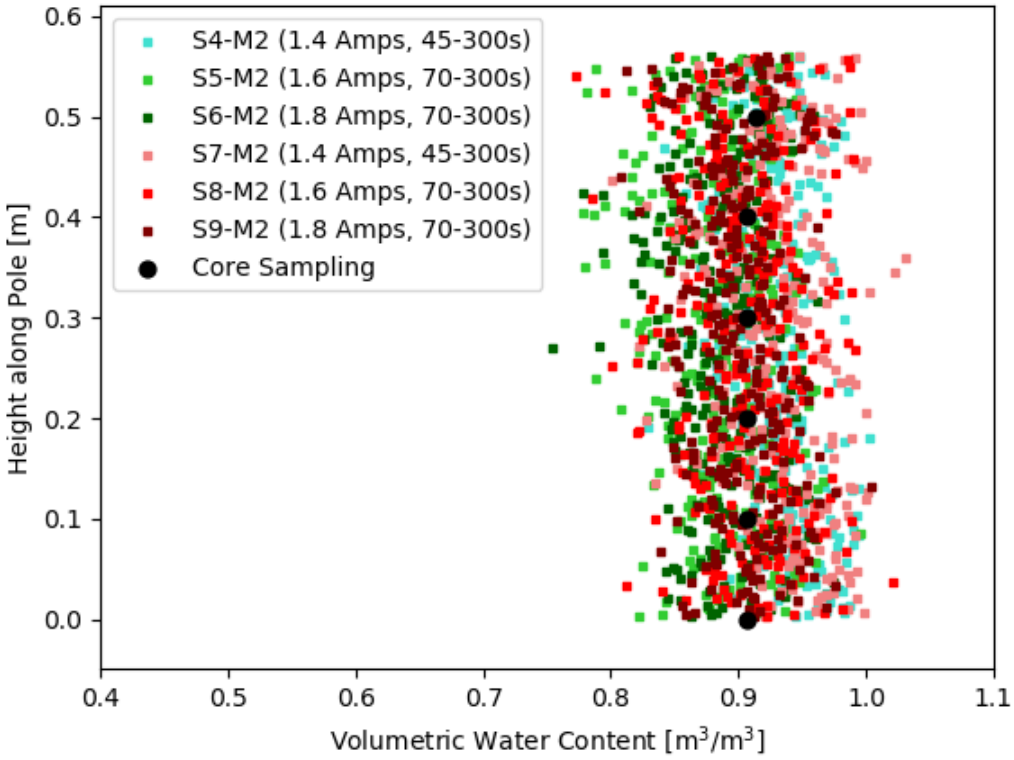

Fig. 29. Volumetric water content for DTS data determined by down-scaling the heat flux with a correction factor of 1.87. DTS data from S4-M2 through to S9-M2 is displayed, with cutoff times at 70s and 300s. Tests S1 and S4 had an earlier cutoff time (45s) because they were the first experiments of the day and therefore had no residual heat in the mud prior to their DTS cycle. VWC (Θ) obtained from core sampling is also visualized (black circles).

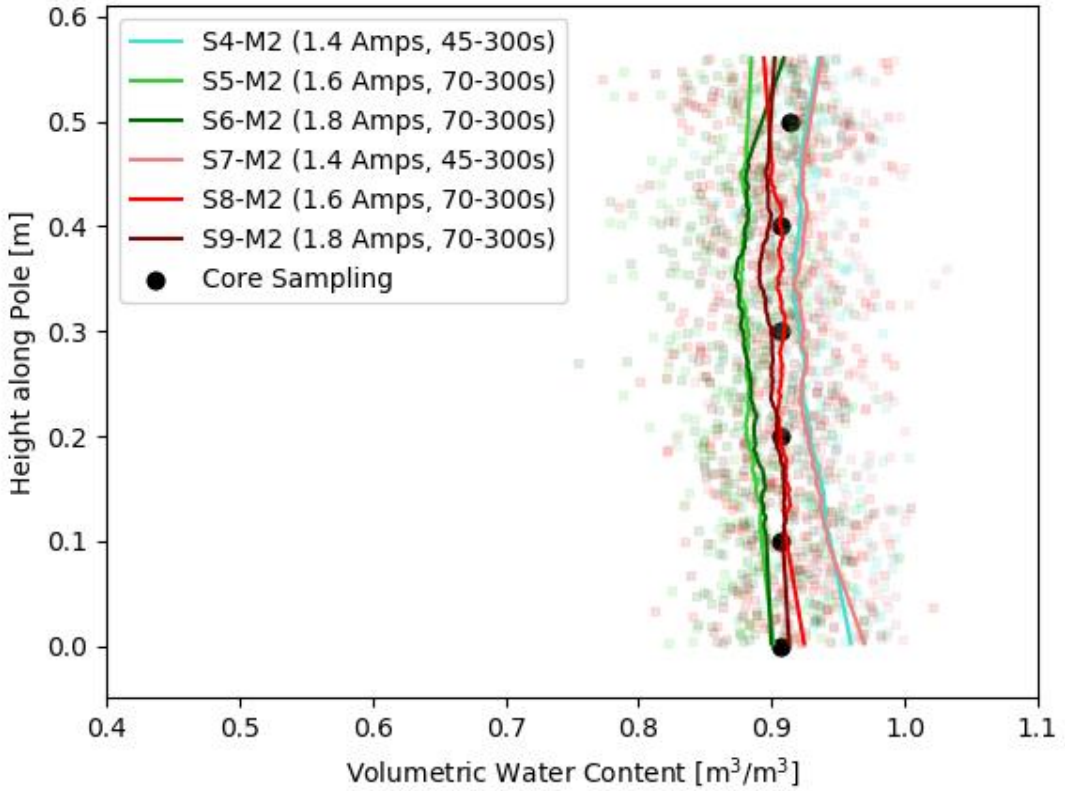

Fig. 30. Smoothed VWC (Θ) results using a Savitzky-Golay filter for tests S4-M2 through to S9-M2. S8 and S9 produce the best individual results when compared to the core sampling VWC's (Θ)

5.3.2 DTS measurements with natural mud from the port of Rotterdam

Mud from the port of Rotterdam was investigated to test the data processing approach on a material typically encountered during an investigation with DTS. Cutoffs in the slope selection procedure were set at 70 seconds and 300 seconds. Table 23 shows results with a comparable degree of coherency in slopes as seen for synthetic muds 1 and 2.

	R4	R7	R5	R8	R6	R9
Peak current [Amps]	1.4		1.6		1.8	
Duration [s]	300	Cutoff at 300	300	Cutoff at 300	300	Cutoff at 300
Date of experiment	07/07	08/07	07/07	08/07	07/07	08/07
Experiment order (daily)	4	1	5	2	6	3
Average slope along depth profile [°C]	2.98	2.88	4.13	4.01	5.02	4.83
Standard deviation [°C]	0.225	0.227	0.269	0.266	0.237	0.237

Table 23. Slopes obtained from the ΔT vs ln(t) plot for tests R4 through to R9 grouped by peak current magnitude. Tests R6-R9 were cut at 300s so that only the mid-section of the curve was used for slope calculations.

From Table 24, the correction factors predicted from tests on the natural mud are lower than those of the synthetic muds (average 1.71 vs 1.87). A likely cause being its variable composition and solid thermal different conductivity.

	R4	R7	R5	R8	R6	R9
Peak current [Amps]	1.4		1.6		1.8	
Calculated heat flux [W m^{-1}]	55.8		72.9		92.2	
Duration [s]	300	Cutoff at 300	300	Cutoff at 300	300	Cutoff at 300
Predicted heat flux* [W m^{-1}]	32.3	31.2	44.8	43.5	54.4	52.4
Calculated thermal conductivity [W m^{-1} K^{-1}]	1.50	1.55	1.41	1.45	1.46	1.52
Predicted thermal conductivity [W m^{-1} K^{-1}]	0.88	0.83	0.82	0.85	0.86	0.91
Correction factor	1.73	1.79	1.63	1.68	1.69	1.76

Table 24. A comparison of the heat flux calculated from the geometry and peak current applied to the set-up vs the heat flux predicted from back-calculation with the core sampling VWC (Θ) in equation (25) and the linear regression of equation (9). Subsequently, calculated and predicted thermal conductivities are also shown, as well as the factor difference between them (correction factor). For reference, the thermal conductivity of R obtained by thermal needle probe was 0.86 W m^{-1} K^{-1}.

The correction factor applied to the heat pulse *q* therefore seems to be dependent on the type of mud tested. After processing the natural mud data using its correction factor (1.71), the VWC's *(Θ)* may be observed in Table 25 and illustrated in Fig. 31.

	R4	R7	R5	R8	R6	R9		
Peak current [Amps]	1.4		1.6		1.8			
Date	07/07	08/07	07/07	08/07	07/07	08/07		
Experiment order (daily)	4	1	5	2	6	3	**Average VWC (*Θ*) across experiments [$m^3\ m^{-3}$]**	**Core sampling average VWC (*Θ*) [$m^3\ m^{-3}$]**
Average VWC (*Θ*) along depth profile [$m^3\ m^{-3}$]	0.767	0.746	0.804	0.785	0.779	0.756	0.773	0.774
Standard deviation [$m^3\ m^{-3}$]	0.046	0.048	0.040	0.040	0.029	0.030	0.039	0.006

Table 25. Natural mud VWC (Θ) obtained by down-scaling the calculated heat flux by the average correction factor (1.71). Average VWC (Θ) determined by core sampling is also printed for comparison.

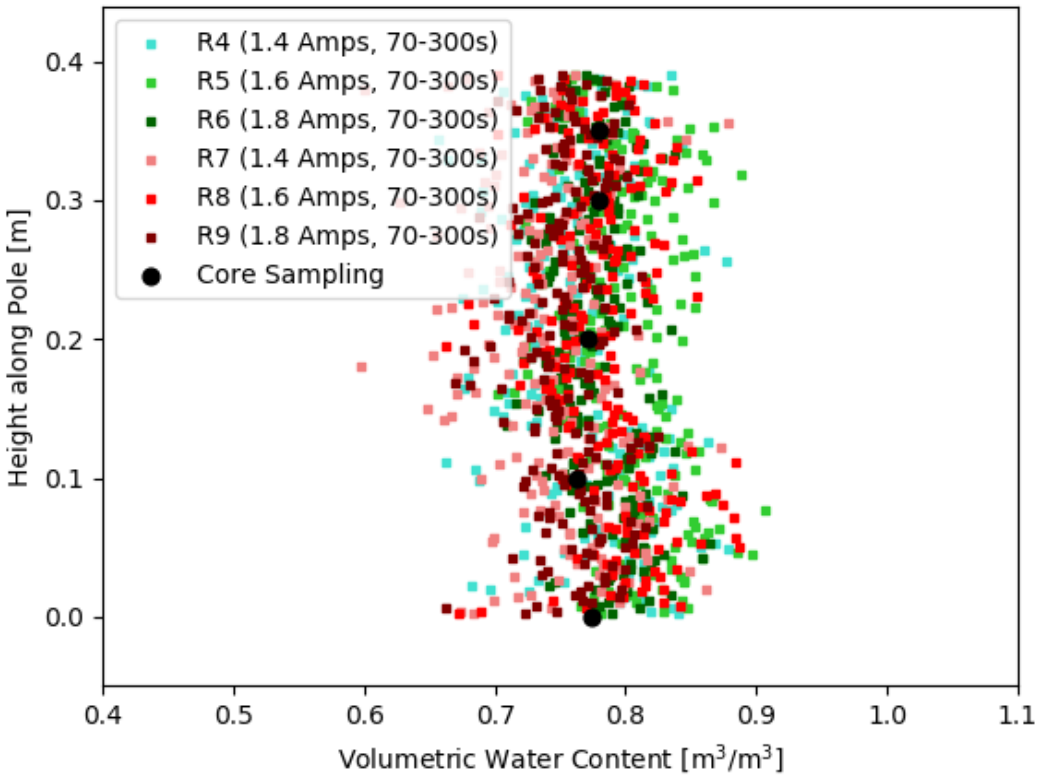

Fig. 31. Volumetric water content for DTS data determined by down-scaling the heat flux with a correction factor of 1.71. DTS data from S4-M2 through to S9-M2 is displayed, with cutoff times at 70s and 300s. VWC (Θ) obtained from core sampling is also visualized (black circles).

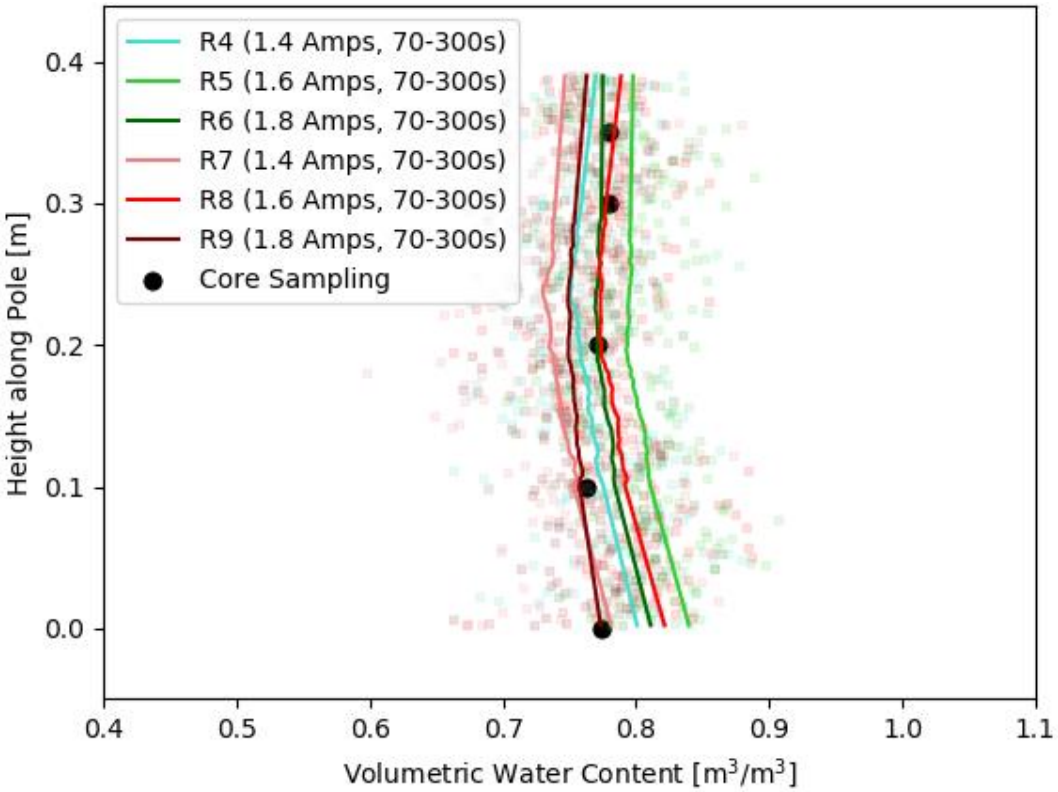

Fig. 32. Smoothed VWC (Θ) results using a Savitzky-Golay filter for tests R4 through to R9. DTS data from R4-M2 through to S9-M2 is displayed, with cutoff times at 70s and 300s.

Once again, the VWC's (Θ) determined with the approach developed are in excellent agreement with those determined from core sampling (average of 0.773 vs 0.774 respectively). From Fig. 32, no single heating strategy can conclusively be declared superior to any of the others. Instead, a combination of the results from multiple tests is preferred.

6. Conclusion & Recommendations

This research has established a step-by-step testing and data processing approach that achieves continuous measurement of water content from AHFO-DTS data. The investigation was focused on a laboratory setting featuring muds that are less dynamic (negligible compaction).

In the $\Delta T \rightarrow \lambda$ model step, an early- and late-time cutoff are introduced to the $\Delta T \; vs \; \ln(t)$ relationship. The early-time cutoffs are individually selected for every test performed and the late-time cutoffs are set at 300 seconds. Linear regression of the section bounded by the cutoffs is then used to obtain the slopes, from which mud thermal conductivity is eventually derived. By isolating the slope from the section of the curve where thermal conductivity effects are expected to dominate, a more accurate result in mud thermal conductivity is expected. In the $\lambda \rightarrow \theta$ model step, a heat flux correction factor is applied to account for the non-negligible thermal conductivity of the set-up. This factor was shown to be both set-up and mud-type dependent (1.87 for synthetic muds, 1.71 for mud from the port of Rotterdam).

It was discovered that when considering individual heating strategies, it may be stated that larger heat pulse magnitudes and longer durations (>150 seconds) feature a larger S/N ratio and therefore produce less variance in the VWC (Θ) results. However, findings from all three tested muds indicate a combination of data from multiple heating strategies spatially averaged may produce volumetric water contents most closely resembling those obtained by conventional methods (core sampling). Furthermore, by applying FO cables in a set-up with a larger bend radius (larger pole and longer coils), the variance in recorded temperatures may be reduced, promoting better precision in processed data derived from these temperatures (thermal conductivity and ultimately volumetric water content).

The data processing approach described yields VWC's (Θ) that are in very good agreement with independent core sampling results. For synthetic mud 1, this was 0.878 m^3m^{-3} from DTS vs 0.879 m^3m^{-3} from core sampling, with a standard deviation of 0.029 m^3m^{-3}. For synthetic mud 2, this was 0.908 m^3m^{-3} from DTS vs 0.908 m^3m^{-3} from core sampling, with a standard deviation of 0.037 m^3m^{-3}. For natural mud from the port of Rotterdam, this was 0.773 m^3m^{-3} from DTS vs 0.774 m^3m^{-3} from core sampling, with a standard deviation of 0.039 m^3m^{-3}.

It is proposed that the procedure established is applied in future work according to the following steps. Prior to field tests, small-scale laboratory experiments can be performed to determine mineral content characterization and thermal conductivity of the mud. Core samples should then be taken to obtain an accurate reference of VWC (Θ) which is in turn used to determine the correction factor in q by back calculating using equation (9) and equation (25). A relatively accurate and continuous VWC (Θ) profile is then derived from DTS data, with a standard deviation of between 0.03 - 0.04 m^3/m^3. Rather than predicting exact VWC's (Θ) it is therefore more reliable as a guideline on volumetric water content in saturated mud (see Fig. 33 in Appendix I for a flowchart of the steps involved). In practice, these results show great promise at achieving continuous volumetric water content measurements at a relatively low cost and virtually no safety issues in a saturated setting.

Recommendations for the future are the following:

1) Although the investigation was able to observe interfaces (layering) and compaction, it was outside the scope of the research. It would be important to incorporate these aspects in future investigations performed.

2) Perform several experiments of varying heat flux magnitudes and durations. Testing several durations will aid in the optimization of the cutoff selection procedure. Averaging VWC's (Θ) from several tests with varying heat flux magnitudes produces more accurate results than any individual test.

3) Although unnecessary for short FO lengths, it is suggested that future work is calibrated with a double-ended approach. The exact calibration would likely yield more accurate VWC's (Θ).

4) Expand the range of muds tested so that the procedure developed can be verified on more dynamic mud types. This would also shed light on the impact of mud type on the correction factor applied to the heat flux.

5) Use a sufficiently large diameter support pole that enables looser winding of the FO cable to avoid macrobending and mitigate the variance in DTS temperatures recorded.

6) Perform a quantitative analysis of the effect of the thermal conductivities of the set-up components and verify their effect on the heat pulse correction factor. (modeling)

7) The correction factor for heat flux is dependent on the mud type and on the set-up itself. In the field, every new mud layer or mud type encountered should be sampled and tested in the lab, so that a corresponding correction factor is computed for every new soil tested.

8) Design an experimental set-up that allows for the analysis of the volumetric heat capacity of the mud. The relationship between volumetric heat capacity and water content has fewer complexities than the $\lambda - \theta$ approach (grain size/shape/contact, etc.) and is potentially more reliable in a heterogenous field setting.

9) Optimize the heat delivery system: by incorporating the heat element into the FO cable, the amount of material separating the heat source and the mud is reduced, hereby mitigating the effects of the set-up on the heat flux and subsequent thermal response.

References

Apperl, B., Bernhardt, M., & Schulz, K. (2019). Towards Improved Field Application of Using Distributed Temperature Sensing for Soil Moisture Estimation: A Laboratory Experiment. *Sensors*, *20*(1), 29. doi: 10.3390/s20010029

Bakx, W., Doornenbal, P., Weesep, R., Bense, V., Essink, G., & Bierkens, M. (2019). Determining the Relation between Groundwater Flow Velocities and Measured Temperature Differences Using Active Heating-Distributed Temperature Sensing. *Water*, *11*(8), 1619. doi: 10.3390/w11081619

Benítez-Buelga, J., Sayde, C., Rodríguez-Sinobas, L., & Selker, J. (2014). Heated Fiber Optic Distributed Temperature Sensing: A Dual-Probe Heat-Pulse Approach. *Vadose Zone Journal*, *13*(11), vzj2014.02.0014. doi: 10.2136/vzj2014.02.0014

Bristow, K. (2002). 5.3 Thermal Conductivity. *SSSA Book Series*, 1209-1226. doi: 10.2136/sssabookser5.4.c50

Camillo, P., and T. J. Schmugge, 1981: A computer program for the simulation of heat and moisture flow in soils. NASA Tech. Memo. 82121, 93 pp. [Available online at http://ntrs.nasa.gov/ archive/nasa/casi.ntrs.nasa.gov/19830019046.pdf.]

Campbell, G.S.; Calissendorff, C.; Williams, J.H. Probe for Measuring Soil Specific Heat Using a Heat-Pulse Method. *Soil Sci. Soc. Am. J.* 1991, *55*, 291–293.

Cao, D., Shi, B., Zhu, H., Wei, G., Chen, S., & Yan, J. (2015). A distributed measurement method for in-situ soil moisture content by using carbon-fiber heated cable. *Journal Of Rock Mechanics And Geotechnical Engineering*, *7*(6), 700-707. doi: 10.1016/j.jrmge.2015.08.003

Carslaw, H.; Jaeger, J. *Conduction of Heat in Solids*; University Press Oxford: Oxford, UK, 1959.

Ciocca, F., Lunati, I., Van de Giesen, N., & Parlange, M. (2012). Heated Optical Fiber for Distributed Soil-Moisture Measurements: A Lysimeter Experiment. *Vadose Zone Journal*, *11*(4), vzj2011.0199. doi: 10.2136/vzj2011.0199

Côté, J., & Konrad, J. (2005). A generalized thermal conductivity model for soils and construction materials. *Canadian Geotechnical Journal*, *42*(2), 443-458. doi: 10.1139/t04-106

DE VRIES, D. (1952). A NONSTATIONARY METHOD FOR DETERMINING THERMAL CONDUCTIVITY OF SOIL IN SITU. *Soil Science*, *73*(2), 83-90. doi: 10.1097/00010694-195202000-00001

De Vries, D. Thermal properties of soils. In *Physics of Plant Environment*; Van Wijk, W., Ed.; North Holland Publ. Co.: Amsterdam, The Netherlands, 1963; pp. 210–235.

des Tombe, B., Schilperoort, B., & Bakker, M. (2020). Estimation of Temperature and Associated Uncertainty from Fiber-Optic Raman-Spectrum Distributed Temperature Sensing. *Sensors*, *20*(8), 2235. doi: 10.3390/s20082235

Farouki OT (1981) *Thermal properties of soils.* Cold Regions Science and Engineering Laboratory Monograph 81-1, US Army Corps of Engineers

Farouki, O. T (1986) *Thermal Properties of Soils.* Series on Rock and Soil Mechanics, Vol. 11, Trans Tech, 136 pp.

Fiber Optics – LEONI. (2020). Retrieved 5 August 2020, from https://www.leoni-fiber-optics.com/

GmbH, A. (2020). AP Sensing | Fiber Optic Distributed Temperature Sensing. Retrieved 5 August 2020, from https://www.apsensing.com/

Hausner, M., Suárez, F., Glander, K., Giesen, N., Selker, J., & Tyler, S. (2011). Calibrating Single-Ended Fiber-Optic Raman Spectra Distributed Temperature Sensing Data. *Sensors*, *11*(11), 10859-10879. doi: 10.3390/s111110859

Hartog, A. (1983). *A distributed temperature sensor based on liquid-core optical fibers*. Journal of Lightwave Technology, 1 (3): 498-509.

He, H., Dyck, M., Horton, R., Ren, T., Bristow, K., Lv, J., & Si, B. (2018). Development and Application of the Heat Pulse Method for Soil Physical Measurements. *Reviews Of Geophysics*, *56*(4), 567-620. doi: 10.1029/2017rg000584

Jay, J.A. (2011). An Overview of Macrobending and Microbending of Optical Fibers.

Johansen, O. Thermal conductivity of soils. Ph.D. diss. Norwegian Univ. of Science and Technol., Trondheim (CRREL draft transl. 637, 1977). 1975.

Kersey, A. (2000). *Optical Fiber Sensors for Permanent Downwell Monitoring Applications in the Oil and Gas Industry*. IEICE Trans. Electron., Vol. E83-C (3).

Kirichek, A., Rutgers, R., Wensween, M., & Van Hassent, A. (2019). *Sediment management in the Port of Rotterdam* [Ebook].

Kluitenberg, G., Ham, J., & Bristow, K. (1993). Error Analysis of the Heat Pulse Method for Measuring Soil Volumetric Heat Capacity. *Soil Science Society Of America Journal*, *57*(6), 1444-1451. doi: 10.2136/sssaj1993.03615995005700060008x

Kluitenberg, G., Bristow, K., & Das, B. (1995). Error Analysis of Heat Pulse Method for Measuring Soil Heat Capacity, Diffusivity, and Conductivity. *Soil Science Society Of America Journal*, *59*(3), 719-726. doi: 10.2136/sssaj1995.03615995005900030013x

Kluitenberg, G. (2002). 5.2 Heat Capacity and Specific Heat. *SSSA Book Series*, 1201-1208. doi: 10.2136/sssabookser5.4.c49

Knight, J., & Kluitenberg, G. (2004). SIMPLIFIED COMPUTATIONAL APPROACH FOR DUAL-PROBE HEAT-PULSE METHOD. *Soil Science Society Of America Journal*, *68*(2), 447-449. doi: 10.2136/sssaj2004.4470

Lu, S., Ren, T., Gong, Y., & Horton, R. (2007). An Improved Model for Predicting Soil Thermal Conductivity from Water Content at Room Temperature. *Soil Science Society Of America Journal*, *71*(1), 8-14. doi: 10.2136/sssaj2006.0041

Nagy, B., 2014. Comparison of Approximate Soil Thermal Conductivity Calculations with Laboratory Measurements and New Estimation Methods for Sandy Clayey Silt. *Advanced Materials Research*, 1041, pp.281-287.

Nikoosokhan, S., Nowamooz, H., & Chazallon, C. (2015). Effect of dry density, soil texture and time-spatial variable water content on the soil thermal conductivity. *Geomechanics And Geoengineering*, *11*(2), 149-158. doi: 10.1080/17486025.2015.1048313

Sakaki, T., Firat Lüthi, B., Vogt, T., Uyama, M., & Niunoya, S. (2019). Heated fiber-optic cables for distributed dry density measurements of granulated bentonite mixtures: Feasibility

experiments. *Geomechanics For Energy And The Environment*, *17*, 57-65. doi: 10.1016/j.gete.2018.09.006

Sayde, C., Buelga, J., Rodriguez-Sinobas, L., El Khoury, L., English, M., van de Giesen, N., & Selker, J. (2014). Mapping variability of soil water content and flux across 1-1000 m scales using the Actively Heated Fiber Optic method. *Water Resources Research*, *50*(9), 7302-7317. doi: 10.1002/2013wr014983

Sayde, C., Gregory, C., Gil-Rodriguez, M., Tufillaro, N., Tyler, S., & van de Giesen, N. et al. (2010). Feasibility of soil moisture monitoring with heated fiber optics. *Water Resources Research*, *46*(6). doi: 10.1029/2009wr007846

Selker, J., Thévenaz, L., Huwalk, H., Mallet, A., Luxemburg, W., van de Giesen, N., Stejskal, M., Zeman, J., Westhoff, M., and Parlange, M.B. (2006a). Distributed fiber-optic temperature sensing for hydrologic systems. Water Resour. Res., 42 (2006) W12202.

Selker, J., van de Giesen, N., Westhoff, M., Luxemburg, W., and Parlange, M.B. (2006b). Fiber optics opens window on stream dynamics. Geophys. Res. Lett., 33, L24401.

Shiozawa, S.; Campbell, G.S. Soil thermal conductivity. *Remote Sens. Rev.* 1990, *5*, 301–310.

Steele-Dunne, S., Rutten, M., Krzeminska, D., Hausner, M., Tyler, S., & Selker, J. et al. (2010). Feasibility of soil moisture estimation using passive distributed temperature sensing. *Water Resources Research*, *46*(3). doi: 10.1029/2009wr008272

Striegl, A., & Loheide II, S. (2012). Heated Distributed Temperature Sensing for Field Scale Soil Moisture Monitoring. *Ground Water*, *50*(3), 340-347. doi: 10.1111/j.1745-6584.2012.00928.x

Suárez, F., Hausner, M. B., Dozier, J., Selker, J., Tyler, S. (2011). Heat transfer in the environment: development and use of fiber-optic distributed temperature sensing. Developments in Heat Transfer, 31 (2011): 611-636.

Tyler, S., Selker, J., Hausner, M., Hatch, C., Torgersen, T., Thodal, C., & Schladow, S. (2009). Environmental temperature sensing using Raman spectra DTS fiber-optic methods. *Water Resources Research*, *45*(4). doi: 10.1029/2008wr007052

Vidana Gamage, D., Biswas, A., Strachan, I., & Adamchuk, V. (2018). Soil Water Measurement Using Actively Heated Fiber Optics at Field Scale. *Sensors*, *18*(4), 1116. doi: 10.3390/s18041116

Weiss, J. (2003). Using Fiber Optics to Detect Moisture Intrusion into a Landfill Cap Consisting of a Vegetative Soil Barrier. *Journal Of The Air & Waste Management Association*, *53*(9), 1130-1148. doi: 10.1080/10473289.2003.10466268

Appendices

Appendix I – Data Processing Approach

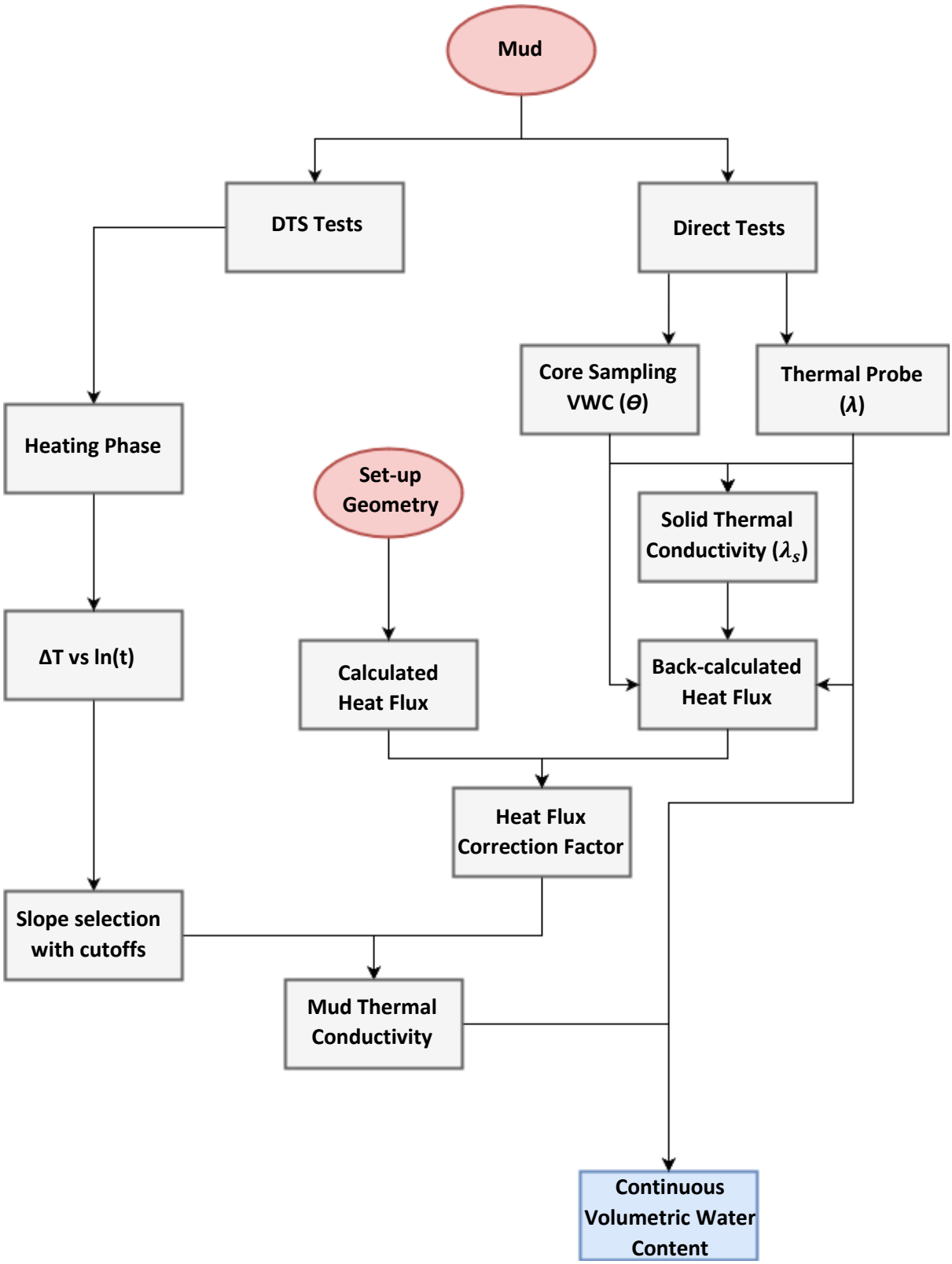

Fig. 33. Data processing approach. All the important steps taken from when a new mud-type is discovered to computing the continuous profile of the volumetric water content in place.